Computational Modeling of the Impact Response of Roma Plastilina Across a Wide Range of Strain Rates

by

Bradley James Walcher Jr.

B.S., Massachusetts Institute of Technology (2017)

Submitted to the Department of Aeronautics and Astronautics
in partial fulfillment of the requirements for the degree of

Master of Science in Aeronautics and Astronautics

at the

MASSACHUSETTS INSTITUTE OF TECHNOLOGY

June 2019

Signature redacted

Author . . . .
Department of Aeronautics and Astronautics
May 22, 2019

Signature redacted

Certified by . . . .
Raúl Radovitzky
Professor of Aeronautics and Astronautics
Thesis Supervisor

Signature redacted

Accepted by . . . .
Sertac Karaman
Associate Professor of Aeronautics and Astronautics
Chair, Graduate Program Committee
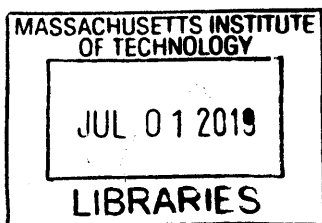
Computational Modeling of the Impact Response of Roma Plastilina Across a Wide Range of Strain Rates

by

Bradley James Walcher Jr.

Submitted to the Department of Aeronautics and Astronautics
on May 22, 2019, in partial fulfillment of the
requirements for the degree of
Master of Science in Aeronautics and Astronautics

Abstract

It has long been known current helmet test methodology suffers from a missing connection between helmet test standards and the relevance to injury prevention. One of the tests in the protocol consists of impacting the helmet material plates with a high-velocity projectile and the performance assessment is based on the permanent deformation of the backing-material, Roma Plastilina clay. This work focuses on the development of a computational framework to develop a deeper understanding of the mechanical response of Roma Plastilina clay. Prior work has focused on the development of a clay model based on Cam-clay theory. In this work, it is shown this model failed to adequately capture the mechanical response across the range of strain rates of interest. To address this deficiency, the previous model formulation is extended to a more general rate-dependence model of the power-law type. Three impact tests are used to calibrate the modified constitutive model for the clay: one low-velocity test and two high-velocity tests. The low-velocity test is a drop test used to ensure the clay is well-conditioned for the high-velocity tests in which a high-velocity projectile impacts a plate with a clay backing. The final clay deformation for all three tests is compared against experimental data to ensure the accuracy of the clay model. Finally, to improve simulation efficiency, scalability of the computational framework is tested. It is concluded the computational framework is an effective tool for modeling Roma Plastilina clay. The constitutive model for the Roma Plastilina clay is validated, tested and final material parameters are determined that characterize the clay behavior over a large range of impact rates. The modified clay model is used to explore the phenomenon of separation between the plate and clay which was previously believed to only occur with hard plate materials.

Thesis Supervisor: Raúl Radovitzky
Title: Professor of Aeronautics and Astronautics

Acknowledgments

So many individuals have had a hand in my success over the years, without them this work could not have been completed. There are some I feel need to have their support acknowledged.

First, I want to thank my research advisor Professor Raul Radovitzky for the opportunity to work on incredible research. Over the years, his guidance and support has helped me through tough decisions and helped me grow into the engineer that I am today. I cannot thank him enough for that. Working within his group at the Institute for Soldier Nanotechnology helped me grow as a researcher and taught me something new every day.

Also, I would like to thank the members of the group, Dr. Bianca Giovanardi, Anwar Koshakji, Adam Sliwiak, Zhiyi Wang and Alex Mijailovic for their support and friendship. Throughout my time in the group they were always available to help answer questions and provide insight.

This work was conducted under the sponsorship of the U.S. Army Program Executive Office of Soldier Protection and Individual Equipment, U.S. Army Natick Soldier Research, Development and Engineering Center and the Institute for Soldier Nanotechnology and I am grateful for their support. I would also like to say thank you to the program manager, Ben Fasel, for his support and direction on this project. Ben was always helpful in advising the project and having confidence the group was heading in the right direction.

Also, I would like to thank MIT, with a special thanks to the AeroAstro Department. Since coming onto campus six years ago, to now finishing graduate school, I have been shaped by the institute and the people around me. I thank MIT and the various people who have helped me see what I am capable of. Another special thank you to all my friends throughout my time at MIT who have always been there to help balance life, education and research.

Finally, I want to express my gratitude to my parents, sister and girlfriend for providing me with unfailing support and encouragement throughout my years of study and through the process of researching and writing this thesis. This accomplishment, as well as my other accomplishments would not be possible without them.

Thank you.

THIS PAGE INTENTIONALLY LEFT BLANK

Contents

List of Figures

List of Tables

THIS PAGE INTENTIONALLY LEFT BLANK

Chapter 1

Introduction

1.1 Background and Objectives

Over the past 10 years, more than 250,000 cases of traumatic brain injury (TBI) have been documented in service men and women [1]. The high rate of TBI has led to research on how well the helmets protect the service members on the battlefield and how the helmets can be improved. TBI threats for soliders have a wide range including blasts or explosions, bullets, falls and vehicle accidents [2].

To this end, numerous studies have been supported by Program Executive Office Soldier Protection and Individual Equipment (PEO-SPIE). One such study utilized animals to develop transfer functions enabling the creation of human head injury criteria [3]. With a transfer function, an estimate can be created to determine the intensity of a threat causing head trauma with a particular protection system. Additional research has been pursued by the US Army Research Laboratory (ARL) to better understand the properties of the helmet materials and the mechanical functions that occur during impact. These studies have shown the dependence and sensitivity of critical material parameters to provide guidance for improved ballistic protection [4].

Although work has been done modeling helmets and creating transfer functions, a crucial step in fulfilling the vision of a complete science-based approach to helmet design and testing is missing. This step involves establishing a connection between helmet testing standards and their relevance for injury prevention. In order to address this question, the testing

methods need to be evaluated to ensure the results are truly measuring the desired effects. This should ensure that helmets that pass a test standard will actually improve soldier safety.

To better understand the testing methods, the objective of this work is to develop simulation and analytical tools to assist Project Manager Soldier Protection and Individual Equipment (PM-SPIE) in the validation or invalidation of current helmet test methodology using existing test data. A validated computational framework is needed that can reproduce experimental results conducted in the past by PM-SPIE. The type of tests considered include those in the standard helmet testing protocol as well as simplified tests. The simplified tests are the main focus of this thesis as they can be used to improve the modeling of the materials used for the overall standard helmet testing protocol. The simplified tests that are used include a drop test and flat-plate high-velocity impacts which are used to calibrate the clay backing-material. The goal of this work is to successfully obtain a Roma Plastilina model that accurately reproduces the results from the experimental tests. Once an accurate model of the materials is obtained, it can be applied to testing and design of new helmets to help reduce the occurrence of traumatic brain injuries.

1.2 Approach

Current helmet test methodology and materials are incorporated into a computational framework to aid in the analysis of materials for various test setups. In order to model the experiments used in the helmet test protocol, each individual material and configuration must be implemented, calibrated and tested as discussed in detail in this work. The final result of this work is a Roma Plastilina clay parameter set that has been calibrated over a large variation in strain rate from quasi-static to high velocity.

The first major step is the model of the Roma Plastilina used in all experimental tests. To accurately model the helmet test protocol, Roma Plastilina clay must be modeled using a single set of material parameters for a large range of impact velocities (6m/s to 743m/s) which correlates to a wide range of peak strain rates (500/s to 50,000/s). Various implementations and models of Roma Plastilina have been pursued, but have focused on either a single strain rate or a smaller range of strain rates [5, 6, 7, 8]. Some work by Carton looked at strain

rates from 0.1/s to 10,000/s but found the material parameters were a function of the strain rate requiring varying stiffnesses to match experimental results [9]. Modeling the Roma Plastilina for this work requires the implementation of material-specific constitutive models which are able to produce accurate results over a wide range of strain rates using a single set of parameters to characterize the material. The approach used is the variational Cam-clay theory of plasticity proposed by Ortiz and Pandolfi [10] which is discussed in detail in Chapter 2. The Cam-clay theory comes from observations of soil in laboratory tests showing soils, when loaded, will reach a critical state in which they are able to sustain plastic deformation at constant volume [10]. Prior work on the implementation of the Cam-clay theory found the constitutive model could be calibrated for a singular strain rate [11]. However, while simulating different strain rates, it was found this constitutive model does not adequately characterize the full range of strain rates. Within Chapter 2, a modification to the rate dependency of the Cam-clay theory is proposed and implemented in order to allow for the material to be characterized by one parameter set for a variety of strain rates. The modification involved changing the linear rate-dependence to an arbitrary power-law rate dependence. The adequacy of the Cam-clay model for the purposes of drop and high-velocity tests will be assessed by simulation. The Cam-clay model is deemed appropriate if it captures the back face deformation as seen in experimental high-velocity impact tests (flat plate with clay-backing) and indentation depth for drop tests.

The Dyneema plate used in the high-velocity impact experiments is a complex structure with a high strength-to-weight ratio that involves many layers of oriented polyethylene fibers embedded in a resin matrix [12, 13]. Plate models include a detailed layup and fiber orientation are not computationally efficient leading to simplified homogenized or orthotropic continuum models [4]. To be computationally efficient and for simplicity, the Dyneema plate is modeled by adopting a plasticity model based off J_2-flow theory [14]. The formulation of plasticity model with assumed power-law forms for both hardening and rate sensitivity is discussed in Appendix A. The plasticity model simplifies the Dyneema structure leading to improved computational run-time, however, there is reduced accuracy from the missing characteristics of the layers and fiber orientation [4]. While this plasticity model is already implemented within the computational framework used, the material parameters need to

be calibrated using experimental results to accurately depict the behavior of the particular Dyneema plate configuration used. The model is deemed appropriate if the final back face deformation and shape matches that of the experimental plates from experiments.

The computational framework used for the tasks within this work is discussed in Chapter 3. The continuum mechanics formulation is discussed along with the explicit Newmark solver which is used in all simulations for this work. Additionally, the problems in this work require a projectile to impact either the plate or the clay. This led to the need for a contact algorithm that could be used for both the drop test and high-velocity impact simulations. The contact algorithm allows the projectile to act as a rigid material as discussed in Appendix B and the penalty parameter selection shown in Section 3.2. Looking at experimental plates from the high-velocity impact tests, it is seen that the Dyneema plate undergoes penetration and delamination between the layers. These observations led to the need to model fracture within the plate. The Discontinuous Galerkin (DG) method is used in combination with the cohesive zone model to simulate the fracture and delamination of the plate [15]. Additionally, the DG method allowed for a free boundary between the clay and plate so the two materials could act as they do in the experiments.

In Chapter 4, the Roma Plastilina model is calibrated using the drop test experimental configuration and the high-velocity impact experimental set-up. There are three experimental configurations that are analyzed [16]. The first is a drop test experiment that is used to ensure that the material is properly conditioned for the high-velocity impact experiments. The second experiment involved attaching a plate of Dyneema to the top face of a clay block then launching a 9mm projectile at the plate and measuring the final deformation of the clay material which is related to the maximum back-face deformation of the plate. The third test also involves a plate but the projectile is different and is called a Threat M. Once again, after each experiment the final deformation of the material is measured. The experimental setup as well as the clay deformation will be discussed later but images are shown in Figure 1-1 and Figure 1-2 to provide an initial view of the experimental setups and results. A group of parameter sets are proposed from the drop test experiment. The high-velocity impact experiments are then used to narrow the parameter sets to find a single set that properly characterized the Roma Plastilina for a wide range of impact velocities. At the end of Chap-
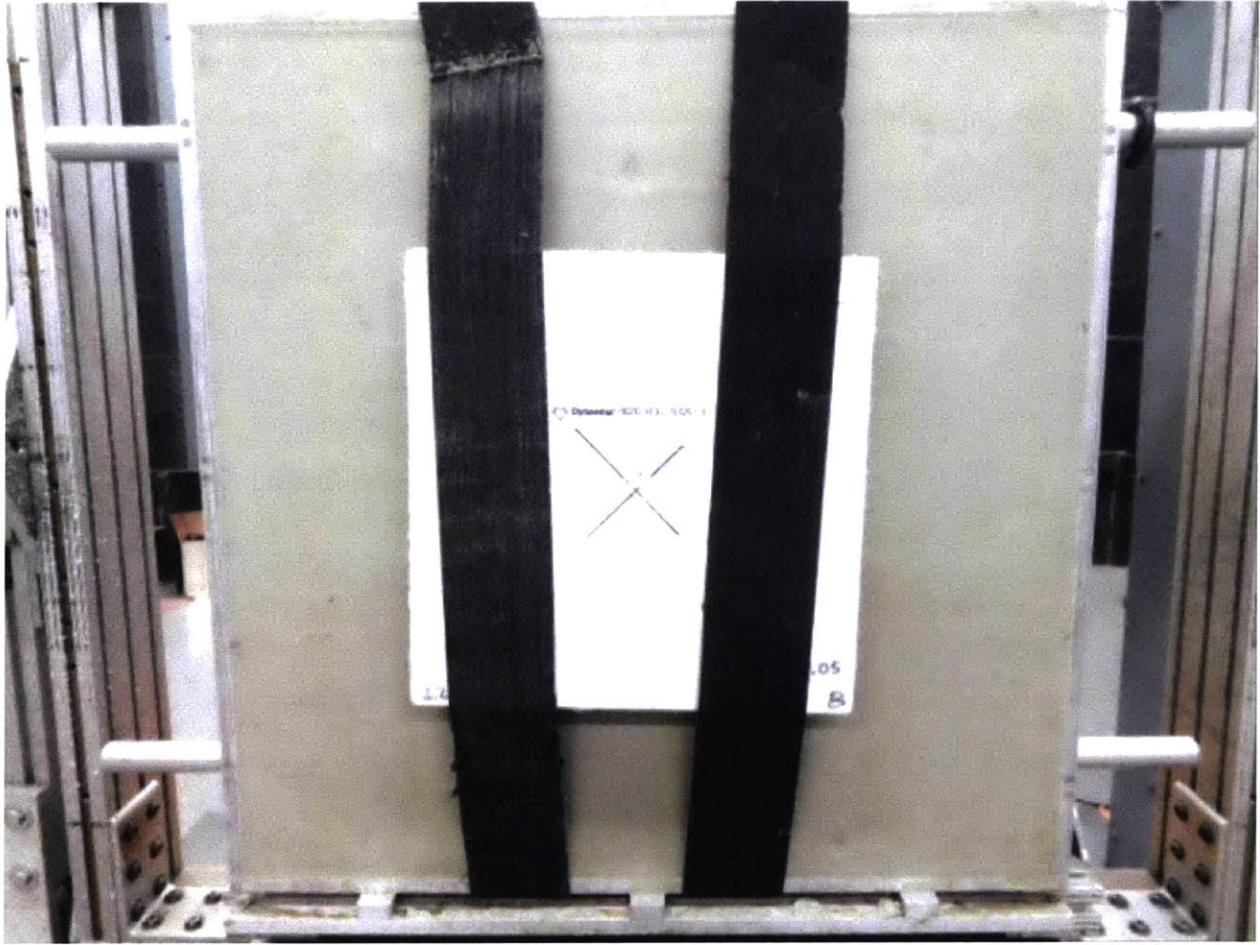
Figure 1-1: Experimental set up for high-velocity impacts

ter 4, the final Roma Plastilina parameters are given which adequately model the material under a wide range of strain rates.

The simulated high-velocity impacts are computationally heavy due to the DG method that increases the number of degrees of freedom compared to the continuous Galerkin (CG) method. The computation time also increases with the cohesive zone model as interface calculations are needed to verify if fracture has occurred. The simulations are run in parallel to reduce the computational time. In order to optimize the parallelization of the simulations, the scalability of the computational framework was tested. Scalability of the simulations is a measure of its capacity to effectively utilize an increasing number of processors and performance statistics are used to guide the design and application of code [17, 18]. To test the scalability, the simulations where run on the ARL Centennial HPC system [19]. The Centennial system has 1,784 compute nodes with 40 cores per node which allows for

(a) Threat M   (b) 9mm

Figure 1-2: Final clay deformation of clay from Threat M and 9mm impacts

simulations to be run on a large number of processors. In order to better understand the number of processors and the size of problem that could be effectively run, a scalability analysis was completed. The results are shown and discussed in Chapter 5, and provide insight into the parallel computing capability of the code with large problem sizes. The analysis of the scalability provides the ability to select the number of computation nodes optimal for a given problem size.

As part of the work with the cohesive zone model, the application of the framework to fragmentation of pressurized tanks was explored. In Chapter 6, a Saturn V helium tank simulation is discussed including the tank mesh, pressurization characteristics and fracture mechanics. The goal of the pressurized tank simulations is to generate a fragmentation catalog which can help determine how many fragments are created due a particular failure.

Chapter 2

Constitutive Model of Roma Plastilina Clay

In order to model the drop test and high-velocity impact experiments, a model of the Roma-Plastilina clay is required. The model used for the clay is a variational Cam-clay theory of plasticity by Ortiz and Pandolfi, which is a variation of the original Cam-clay theory by Scholfield and Worth [10, 20]. The main concepts are derived from observations of soil in laboratory tests and is heavily based on a critical state in which the soil or clay can sustain plastic deformation at constant volume. The constitutive model is discussed in further detail in Section 2.1. While testing different configurations of the clay, it was found that the model did not accurately characterize the material with large ranges of impact velocities (i.e. strain rates). The material could be calibrated to a low strain rate but would act overly stiff for high strain rates or could be calibrated to high strain rates and act too soft for low strain rates. Due to this behavior, the Cam-clay theory is modified to have a power-law rate dependency replace the original linear rate dependency shown in Section 2.2. In Section 2.2, the convergence conditions for this modification, as well as the validation and testing, are also discussed to show consistency with the derivation.

2.1 Summary of Original Model Formulation

For this work, the variational Cam-clay theory of plasticity by Ortiz and Pandolfi is used to model the Roma Plastilina [10]. This theory, as mentioned above, is better suited to model the behavior of Roma Plastilina as compared to other models that rely heavily on metal plasticity theory. The formulation of the original variational Cam-clay theory of plasticity is highlighted below with the major equations. The full formulation, with derivation of the following equations, can be seen in the work by Ortiz and Pandolfi [10]. The implementation of the original variational Cam-clay theory of plasticity into computational framework, as well as testing of the original theory can be seen in the work by Fronk [11].

2.1.1 Governing Equations

To begin, the main assumption in the governing equations is the multiplicative decomposition of the deformation gradient $\boldsymbol{F}$ given by Equation (2.1) where $\boldsymbol{F}^e$ and $\boldsymbol{F}^p$ are the elastic and plastic parts, respectively, of the deformation gradient.

$$\boldsymbol{F} = \boldsymbol{F}^e \boldsymbol{F}^p \tag{2.1}$$

Free Energy

Ortiz and Pandolfi assumed that the elasticity and the specific heat of the material are independent of the preconsolidation pressure leading to the free energy given by Equation (2.2) where W^e is the elastic strain-energy and W^p is the stored energy of cold work [10].

$$A(\boldsymbol{F}, \boldsymbol{F}^p, T, \boldsymbol{q}) = W^e(\boldsymbol{C}^e, T) + W^p(T, \boldsymbol{q}, \boldsymbol{F}^p) \tag{2.2}$$

Focusing on the elastic strain-energy, the volumetric and deviatoric responses are decoupled for simplification giving Equation (2.3) where J^e is the Jacobian of the elastic deformation and $C^{e,dev}$ is the deviatoric elastic right Cauchy-Green deformation tensor.

$$W^e(\boldsymbol{C}^e, T) = W^{e,vol}(J^e, T) + W^{e,dev}(\boldsymbol{C}^{e,dev}, T) \tag{2.3}$$

20

The volumetric and deviatoric components are given by Equations (2.4) and (2.5), respectively, where θ^e is the elastic volumetric strain, K is the isothermal bulk modulus, α_T is the thermal expansion coefficient, T_0 is the reference absolute temperature, ρ_0 is the mass density per unit undeformed volume, C_v is the specific heat. For the deviatoric portion, μ is the shear modulus and e^e is the deviatoric portion of the logarithmic elastic strain.

$$W^{e,\text{vol}}(J^e, T) = \frac{K}{2}\left[\theta^e - 3\alpha_T(T - T_0)\right]^2 + \rho_0 C_v T \left(1 - \log\frac{T}{T_0}\right) \qquad (2.4)$$

$$W^{e,\text{dev}} = \mu|e^e|^2 \qquad (2.5)$$

Flow Rule

The flow rule for this theory is assumed to be the von Mises flow rule shown in Equation (2.6) where ϵ^p is the effective plastic strain and $\boldsymbol{M}$ is a tensor which defines the direction of plastic flow [21].

$$\dot{\boldsymbol{F}}^p \boldsymbol{F}^{p-1} = \dot{\varepsilon}^p \boldsymbol{M} \qquad (2.6)$$

Ortiz and Pandolfi discuss the defining characteristic of the Cam-clay theory being that $\boldsymbol{M}$ can be any symmetric tensor that satisfies the kinematic constraint in Equation (2.7) where α is the internal friction coefficient and $\boldsymbol{M}^{dev}$ is the deviatoric part of $\boldsymbol{M}$ [10].

$$\frac{1}{\alpha^2}(\text{tr}\boldsymbol{M})^2 + \frac{2}{3}\boldsymbol{M}^{\text{dev}} \cdot \boldsymbol{M}^{\text{dev}} = 1 \qquad (2.7)$$

Rate-sensitivity law

The rate-sensitivity law is originally assumed to be a linear rate-sensitivity and is given by the dual kinetic potential in Equation (2.8) where η is a viscosity constant.

$$\psi^* = \frac{\eta}{2}(\dot{\varepsilon}^p)^2 \qquad (2.8)$$

The original rate-sensitivity law will be analyzed and modified in Section 2.2

2.1.2 Yield Criterion and Hardening Rule

Yield Criterion

The yield criterion is given by Equation (2.9) in which p is pressure, q is stress and α is the internal friction angle which is related to the friction angle ϕ by Equation (2.10)

$$q^2 + \alpha^2 (p - p_0)^2 = \sigma_0^2 \tag{2.9}$$

$$\alpha = \frac{6 \sin \phi}{3 - \sin \phi} \tag{2.10}$$

From the yield criterion, the yield surface is generated as shown in Figure 2-1.
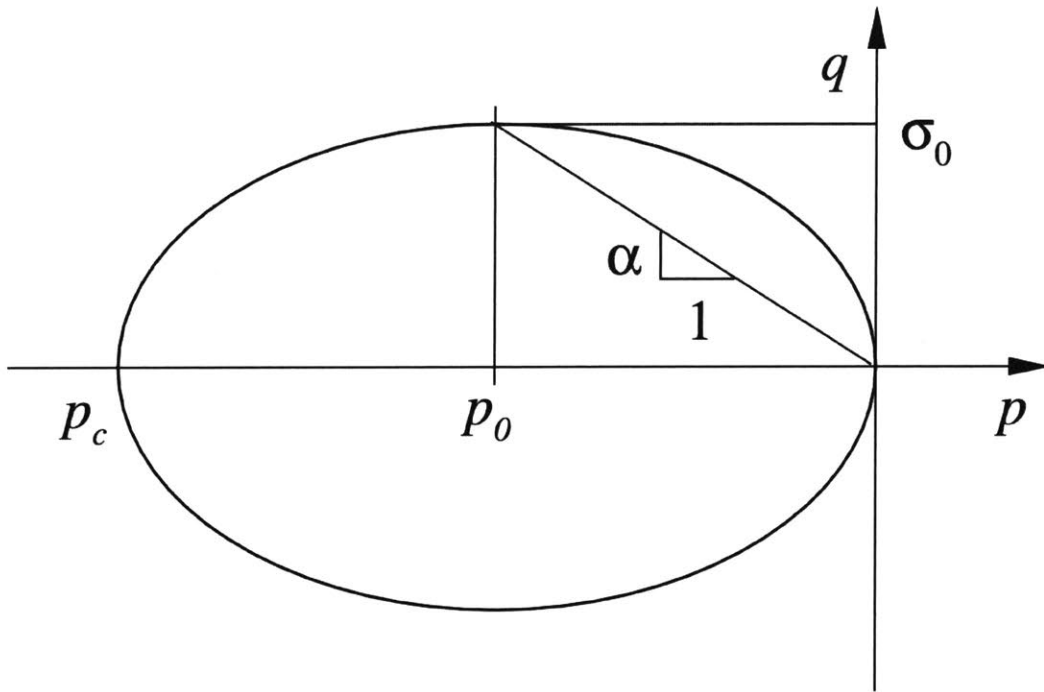

Figure 2-1: Yield surface in the (p, q)-plane, preconsolidation pressure p_c and geometrical interpretation of the internal friction coefficient α

Hardening Rule

The hardening rule for the Cam-clay constitutive model is used to characterize the mechanisms of compression and swelling in granular mediums. The hardening characteristics are

(a) Drop Test Strain Rate
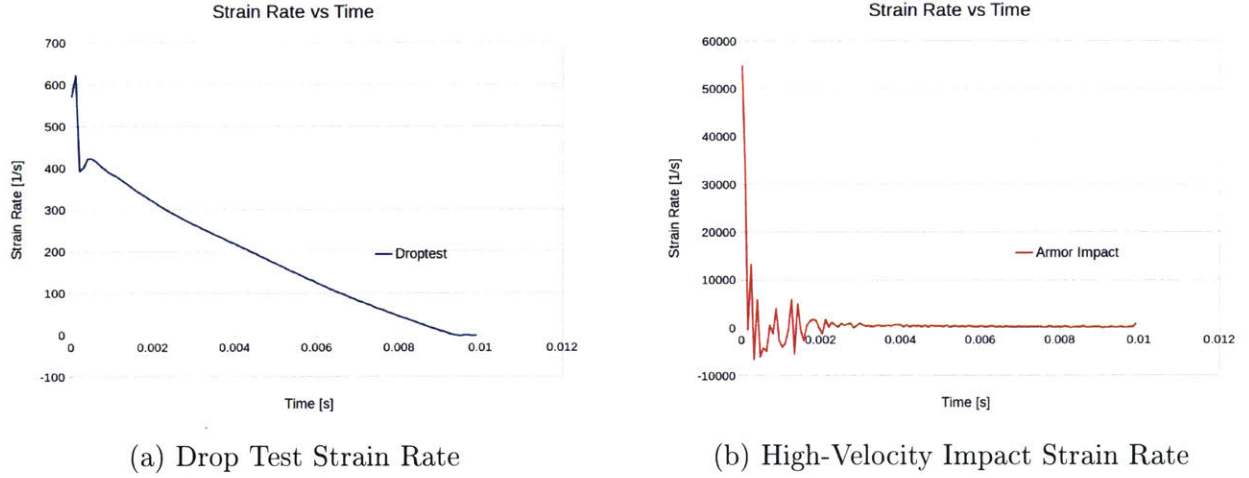

(b) High-Velocity Impact Strain Rate

Figure 2-2: Strain rate versus time of the two main test types analyzed in this work

determined by the normal consolidation relation given by Equation (2.11) where p_{ref} and θ^p_{ref} are material constants.

$$p_c = p_{ref} \sinh \frac{\theta^p}{\theta^p_{ref}} \tag{2.11}$$

The stored energy function corresponding to the normal consolidation relation is given by Equation (2.12) by integrating over the volumetric plastic strain, θ^p.

$$W_c^p(\theta^p) = p_{ref}\theta^p_{ref}\left(\cosh \frac{\theta^p}{\theta^p_{ref}} - 1\right) \tag{2.12}$$

2.2 Power Law Rate Dependence Modification

For the application of the work, the clay is tested over two largely different strain rates. The first strain rate is generated from the drop test experiment in which the ball is dropped at a velocity of approximately 6.3 m/s producing a maximum strain rate of approximately 600 $1/s$ and then tapers down to 0 $1/s$ as the ball is caught in the clay as seen in Figure 2-2a. The second strain rate is from the high-velocity impact tests, in which the clay is topped by the Dyneema plate and then impacted with either a 9mm or Threat M, the maximum strain rate is closer to 55000 $1/s$ and then again tapering to 0 $1/s$ as the bullet gets stopped and the plate separates from the clay as seen in Figure 2-2b.

With the linear rate-sensitivity, the clay is overly rate dependent at high strain rates

23

causing the material to be stiff. To improve the rate dependency, a power law rate dependence was implemented that allows for the ability to use one set of parameters over a wide span of strain rates. The dual kinetic potential for the power law rate-sensitivity is given by:

$$\psi^* = \frac{m\sigma_y\dot{\epsilon}_0^p}{m+1}\left(1 + \frac{\dot{\epsilon}^p}{\dot{\epsilon}_0^p}\right)^{\frac{m+1}{m}}$$
(2.13)

where m is the rate-sensitivity exponent, $\dot{\epsilon}_0^p$ is a reference plastic strain rate, and σ_y is the yield stress which is calculated using the yield criterion. Using the derivation in Section 2.1, the rate-sensitivity term in the original formulation, Equation (2.8), can be replaced with the power law rate-sensitivity, Equation (2.13), directly. This results in a formulation that allows for more control in the strain rate dependency of the Cam-clay material compared to the original formulation.

2.2.1 Power Law Rate-Sensitivity Implementation and Testing

Convergence and Conditions

A Newton-Raphson iteration is used to solve for the incremental plastic strain $\Delta\epsilon^p$ and phase angle ϕ as shown by Ortiz and Pandolfi [10]. The first condition of the power law rate-sensitivity equation is the plastic strain can not be negative so that condition was added to the Newton-Raphson to ensure that at the end of each iteration the value of the plastic strain is positive. Once the power law rate-sensitivity replaced the linear rate-sensitivity equation, the stability of the calculation of the phase angle improved, but began to oscillate with various tests of material parameters. It was determined Newton-Raphson would solve for a particular phase angle with a small change in the angle, but as the incremental plastic strain converged, the phase angle would start to oscillate between angles that varied by a period or more. The same angle was being calculated, but the change in the angle was approximately 2π, leading to the Newton-Raphson not converging for the phase angle. For this reason, a condition was added to the Newton-Raphson that forces the angle to be between 0 and 2π. Once this was implemented, the Newton-Raphson converged to a solution for the incremental plastic strain and the phase angle.

To test the convergence of the Newton-Raphson, a simple hydrostatic compression test
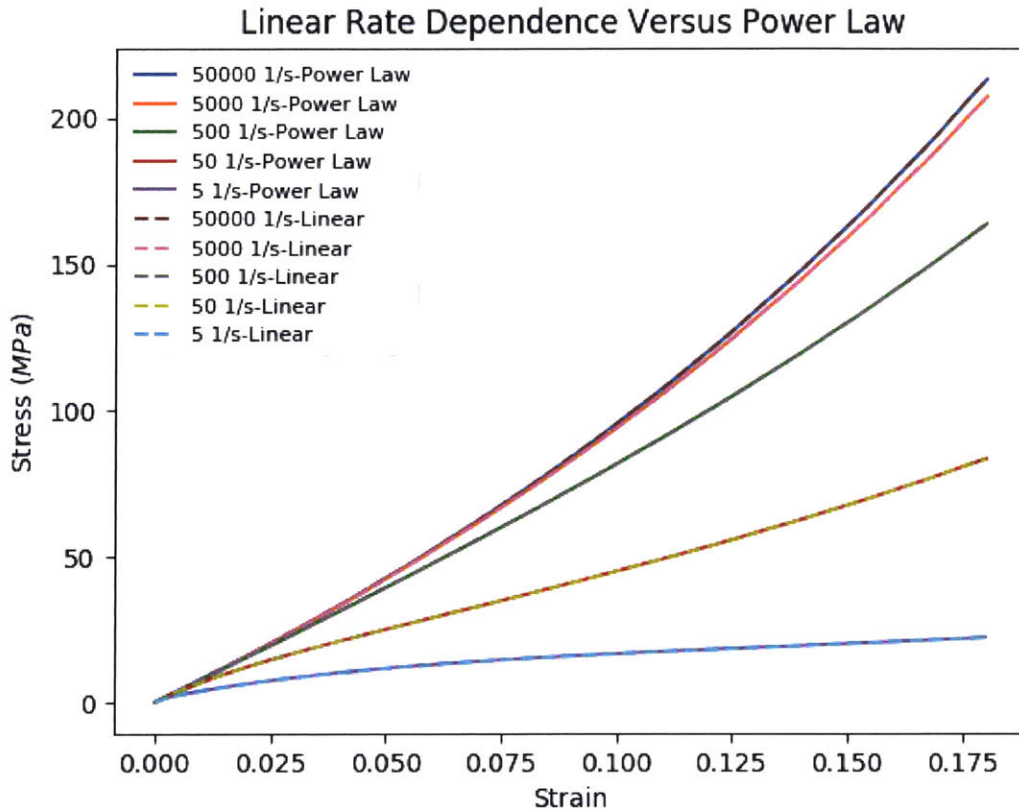
Figure 2-4: Power Law rate-sensitivity overlaid with Linear rate-sensitivity with forced equivalence by setting η in the linear model to be equal to the calculated σ_0. Various strain rates are shown to see that the rate dependency is equal for this comparison

material to equal σ_0 from the power law rate-sensitivity material. Figure 2-4 illustrates that by forcing this equivalence, the power law rate sensitivity overlays the linear rate sensitivity leading to the understanding that the power law rate-sensitivity was implemented correctly.

With the power law rate sensitivity successfully implemented, the compression test can be used to get an understanding of how the new parameters, m and $\dot{\epsilon}_0^P$, impact the rate dependency or behavior of the Cam-clay under various loading rates. In Figure 2-5, the same set of parameters was analyzed while changing the m parameter to discern how the stress is impacted for various strain rates. As m increases, the dependence on the rate begins to reduce. With a large value of m the expectation is that there would be little to no dependence on the strain rate. Figure 2-5 illustrates that as m increases, the material for high strain rates begins to behave like the material at lower strain rates. This includes yielding earlier as well as hardening in the same way. Looking at the derivative of the power
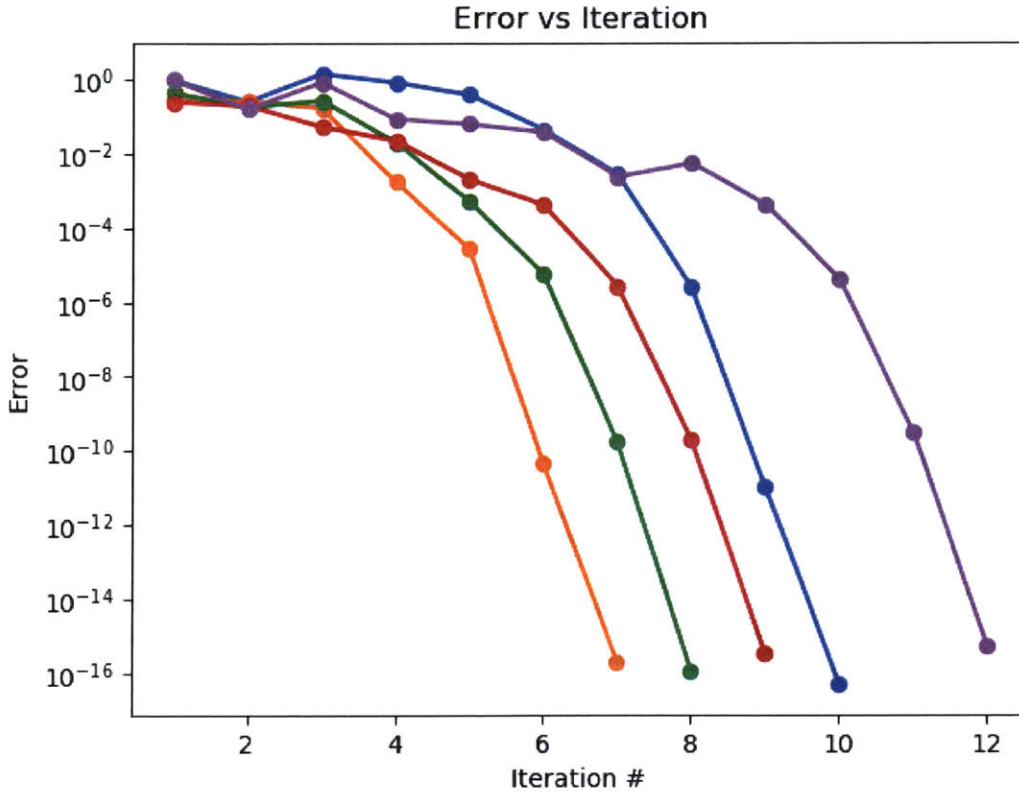
Figure 2-3: Convergence of Newton Raphson while using Power Law rate-sensitivity

was used which involves compressing the material at the same rate in all three principle directions. The convergence at the quadrature point at a random point in time was collected to get a number of samples. This collection of samples gives insight into the overall convergence behavior of the Newton-Raphson. With the added conditions for the Newton-Raphson, the convergence of the iteration is quadratic as is expected for a Newton-Raphson scheme. The convergence is shown in Figure 2-3.

Validation and Testing

As discussed in the work by Fronk, a hydrostatic compression test was used to verify the implementation of the Cam-clay material [11]. The modification to use the power law rate-sensitivity does not have experimental data to verify the implementation other than forcing the linear and power law rate-sensitivities to be equal by setting m and $\dot{\epsilon}_0^P$ to 1, which produces the same equation as long as σ_0 is equal to η. Because σ_0 is calculated using the preconsolidation pressure and the internal friction, η was set in the linear rate-sensitivity

law rate-sensitivity, Equation (2.14), the power of $1/m$ produces this behavior because as m increases, the dependence on the inner term decreases.

$$\sigma = \sigma_y \left(1 + \frac{\dot{\epsilon}^p}{\dot{\epsilon}_0^p}\right)^{\frac{1}{m}} \qquad (2.14)$$

For the reference plastic strain rate, the impact on the behavior of the material can be illustrated using Figure 2-6, in which, m is held constant at 1 but $\dot{\epsilon}_0^p$ is changed. As $\dot{\epsilon}_0^p$ is increased, the magnitude of the stress at higher strain rates decreases as the inner term of Equation (2.14) decreases. Based off the graphs in Figure 2-6, with a high value of $\dot{\epsilon}_0^P$ the stress will converge to the yield stress and maintain that stress as the strain continues to increase. The inner term of Equation (2.14) will approach 1 as $\dot{\epsilon}_0^P$ approaches infinity thus the stress approaches the yield stress, illustrating that the power law rate-sensitivity modification is correctly implemented.
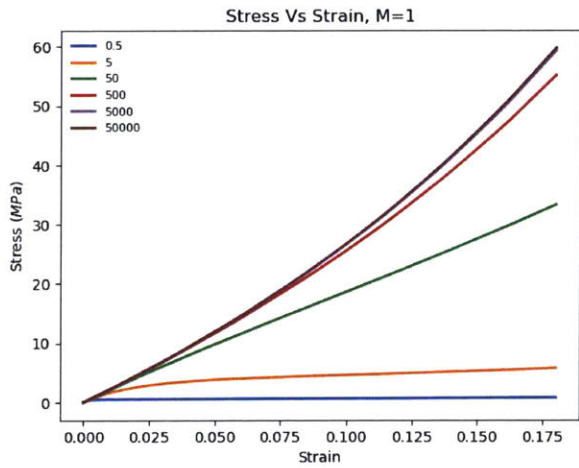
(a) $m = 1$
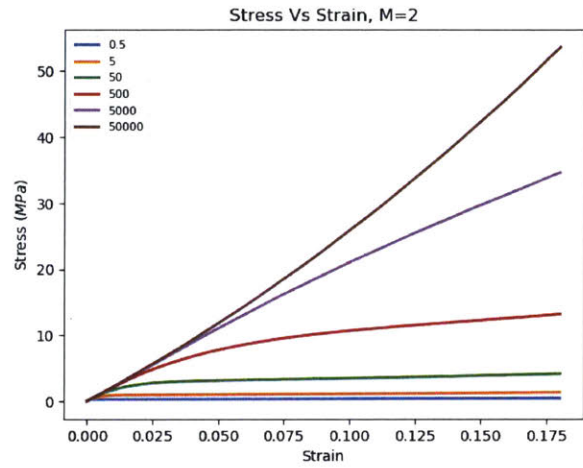
(b) $m = 2$
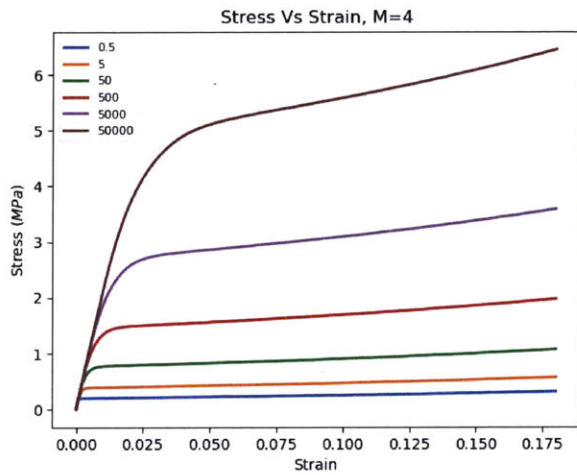
(c) $m = 4$
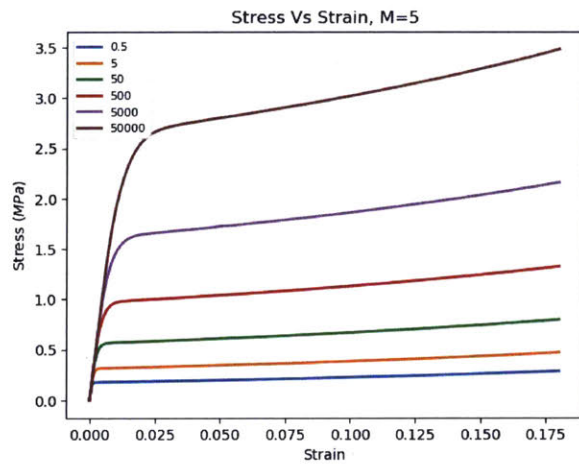
(d) $m = 5$

Figure 2-5: Stress versus strain curves of various strain rates showing the model response for hydrostatic compression test subject to various rate-sensitivity exponents with a fixed reference plastic strain rate of 1.
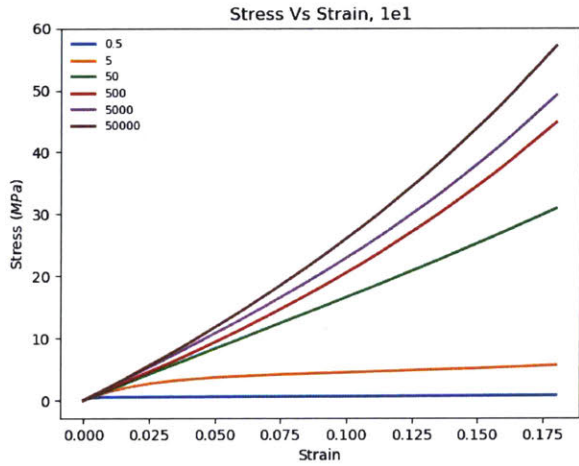
(a) $\dot{\epsilon}_0^p = 1e1$
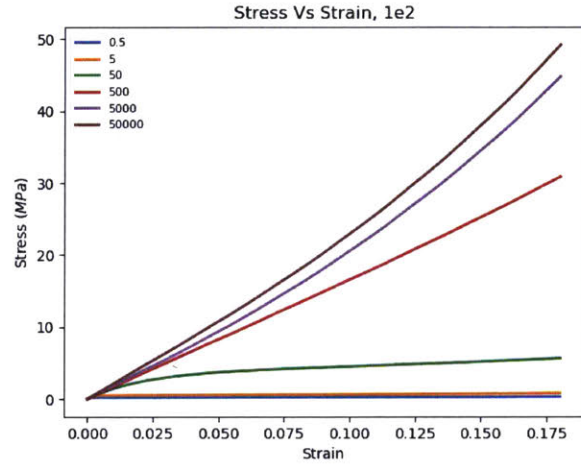
(b) $\dot{\epsilon}_0^p = 1e2$
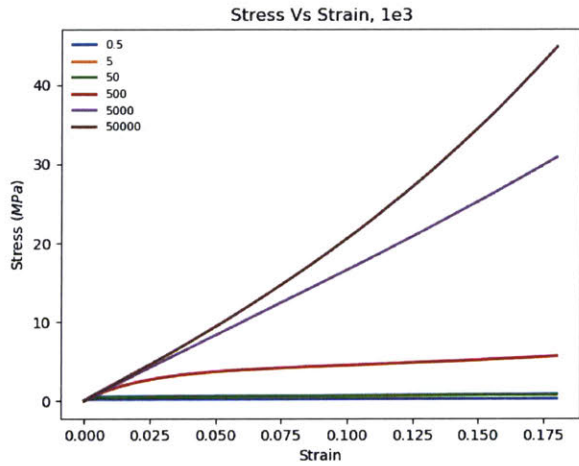
(c) $\dot{\epsilon}_0^p = 1e3$
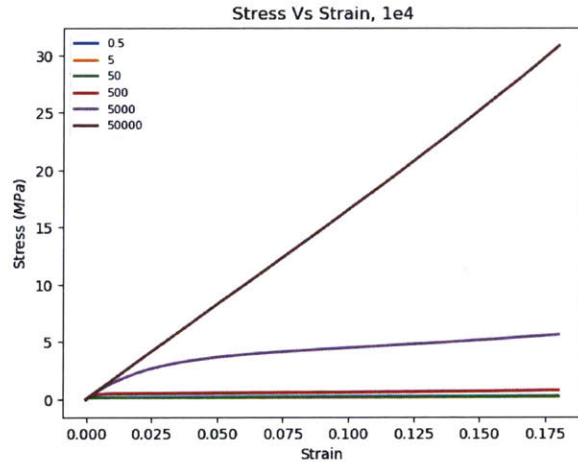
(d) $\dot{\epsilon}_0^p = 1e4$

Figure 2-6: Stress versus strain curves of various strain rates showing the model response for hydrostatic compression test subject to various reference plastic strain rates with a fixed rate-sensitivity exponent of 1.

THIS PAGE INTENTIONALLY LEFT BLANK

Chapter 3

Computational Framework

To simulate and model the test protocols, a computational framework entitled SUMMIT, developed at MIT under the direction of Raul Radovitzky, was used. SUMMIT is a solid mechanics code that is focused on large-scale simulations for materials and structures. The capabilities of the framework, include but are not limited to, continuous and discontiuous Galerkin methods, multi-scale simulations, explicit dynamics and higher order methods [22, 23, 24]. In addition, SUMMIT has a wide variety of constitutive models and the capability to quickly add and test new materials. SUMMIT is also highly scalable, which will be further discussed in Chapter 5, which offers many benefits with highly complex problems. The major features of SUMMIT that are used for the test protocol simulations are discussed below and include the continuum mechanics formulation, the contact algorithm for the projectile, discontinuous Galerkin (DG) method, and the cohesive zone model used for fracture and separation.

3.1   Continuum Mechanics Formulation

The base mathematical formulation for modeling finite deformation is based off deformation of a material and the linear momentum balance equation. The deformation gradient $\boldsymbol{F}$ is the deformation in the current configuration to the reference configuration as shown in Equation (3.1) where X_j is the material point coordinates in the reference geometry, x_i is the material point coordinates in the current configuration, and $\varphi(\boldsymbol{X}, t)$ is the Lagrangian of

the displacement vector. In Equation (3.2), the governing equation of the linear momentum balance is given where ρ_0 is the initial density, $\ddot{\varphi}$ is the acceleration, P is the first Piola-Kirchoff stress tensor and $\boldsymbol{B}$ is the force per unit mass subjected on the body.

$$F_{ij} = \frac{\partial \boldsymbol{x}_i}{\partial \boldsymbol{X}_j} = \frac{\partial \varphi_i}{\partial \boldsymbol{X}_j} \tag{3.1}$$

$$\rho_0 \ddot{\boldsymbol{\varphi}} = \boldsymbol{\nabla}_0 \cdot \boldsymbol{P^T} + \rho_0 \mathbf{B} \text{ in } B_0 \tag{3.2}$$

The first Piola-Kirchhoff stress is determined from the relationship between the PK stress and the Cauchy stress, σ_{ij}, shown in Equation (3.3) where J is the Jacobian derived from the determinant of the deformation gradient.

$$P_{ij} = J\sigma_{ik}F_{kj}^{-T} \tag{3.3}$$

$$J = det\boldsymbol{F} \tag{3.4}$$

The weak form of Equation (3.2) can be determined by multiplying the equation by a test function φ_h and integrating over the domain which produces Equation (3.5) which can be summed over each element in the finite element problem. Within Equation (3.5), $\bar{\boldsymbol{T}}$ is the applied traction.

$$\sum_e \int_B (\rho_0 \ddot{\boldsymbol{\varphi}}_h \cdot \delta\boldsymbol{\varphi}_h + \boldsymbol{P}_h : \nabla_0 \delta\boldsymbol{\varphi}_h) dV = \sum_e \int_B \rho_0 \boldsymbol{B} \cdot \delta\boldsymbol{\varphi}_h dV + \sum_e \int_{\delta_N B} \delta\boldsymbol{\varphi}_h \cdot \bar{\boldsymbol{T}} dS \tag{3.5}$$

This weak form is the basis for continuous Galerkin (CG) methods.

3.2 Contact Algorithm

In this work, high-velocity impacts are modeled and an efficient way of modeling the impactor is needed. The contact algorithm prevents interpentration of objects which come in contact and is used to determine the resulting contact forces. In addition, the contact algorithm allows the impactor to be modeled as a rigid body with mass, without the need of a meshed object. The contact algorithm is needed for the drop test simulations, as well as the high-

velocity impact simulations in Chapter 4. The contact algorithm was implemented in the initial work by Fronk and is summarized in Appendix B [11].

The most important parameter for the contact algorithm is the penalty parameter as discussed in Appendix B. For the application of this project, the penalty parameter is dependent on the problem (type of material and type of impactor) in which it is applied. For the radius of the sphere, the size of the impactor for a given experiment is used which produces the desired undeformable object to impact the various surfaces. For the penalty parameter, two different values are used. For the drop test simulations and the high-velocity impact simulations, discussed in Chapter 4, the penalty parameter used was $4\mathrm{x}10^8$ and $1\mathrm{x}10^{11}$, respectively.

3.3 Description of Fracture - Discontinuous Galerkin and Cohesive Zone Model

3.3.1 Discontinuous Galerkin (DG) Formulation

Discontinuous Galerkin (DG) methods allow for discontinuities within the problem domain which is beneficial in problems where fracture may occur or separation of elements is needed. For the application of the helmet test protocol, the plate and clay need to be able to separate in order to act as they do in experiments. With a continuous Galerkin (CG) method, the two materials must remain in contact throughout the simulation. The elements are not allowed to separate because the formulation is purely continuous. This is not physical as in the experiments, the two materials act separately and are not permanently joined. Employing a DG method for the helmet system allows for this separation between the clay and Dyneema plate.

Another use of the DG method is to model the delamination and fracture within the plate during an impact. The plate used in the experiments has plies and shows some separation between the plies occurring when some plies displace further than others. With a detailed mesh, the damage to the plate can be shown using the DG method. The DG method would allow the impactor to penetrate the plate producing delamination between the plies.

To achieve separation, delamination, and fracture, an explicit-dynamics spatial DG formulation is used. The explicit-dynamics spatial DG formulation for non-linear solid dynamics is discussed in further detail in the work by Noels and Radovitzky but the main points of the formulation are highlighted below [23].

To get the weak form of the problem, the continuum equations are first stated in material form by Equations (3.6),(3.6) and (3.6) with $\boldsymbol{\varphi}$ being the deformation mapping where $\rho_0 : B_0 \to \mathbb{R}_+$ is the initial density, $\dot{\bullet}$ is the partial differentiation with respect to time at a fixed $\mathbf{X}$, $\mathbf{B}$ is a force per unit mass subjected to the body, $\mathbf{P}$ is the first Piola-Kirchhoff stress tensor, $\mathbf{N}$ is the unit surface normal to the reference configuration and the boundary surface ∂B_0 is split into the Dirichlet portion $\partial_D B_0$ and the Neumann portion $\partial_N B_0$. To integrate the system, displacement and velocity initial conditions are needed.

$$\rho_0 \ddot{\boldsymbol{\varphi}} = \nabla_0 \cdot \mathbf{P} + \rho_0 \mathbf{B} \quad \forall t \in T \tag{3.6}$$

$$\boldsymbol{\varphi} = \bar{\boldsymbol{\varphi}} \quad \forall \mathbf{X} \in \partial_D B_0 \quad \forall t \in T \tag{3.7}$$

$$\mathbf{P} \cdot \mathbf{N} = \bar{\mathbf{T}} \quad \forall \mathbf{X} \in \partial_N B_0 \quad \forall t \in T \tag{3.8}$$

To formulate the DG method for a large class of materials, a variational constitutive framework is needed. This framework is discussed in Section 2.1 and Appendix Section A.1.1.

DG discretization

In the DG discretization, Noels and Radovitzky start by defining an admissable test function $\delta\boldsymbol{\varphi}_h \in X_{hc}^k$ [23]. Integration over the body in the reference configuration of Equation (3.6) multiplied by the test function leads to a weak formulation which consists of finding $\boldsymbol{\varphi} \in X_h^k$ and $\mathbf{P}_h \in S_h^k$ such that Equation (3.9) holds [23].

$$\sum_e \int_{\Omega_0^e} (\rho_0 \ddot{\boldsymbol{\varphi}}_h - \nabla_0 \cdot \boldsymbol{P}_h) \cdot \delta\boldsymbol{\varphi}_h dV = \sum_e \int_{\Omega_0^e} \rho_0 \boldsymbol{B} \delta\boldsymbol{\varphi}_h dV \quad \forall \delta\boldsymbol{\varphi}_h \in X_{hc}^k \quad \forall t \in T \tag{3.9}$$

With Equation (3.8) and the test function, the divergence theorem can be applied to produce Equation (3.10).

$$\sum_e \int_{\Omega_0^e} (\rho_0 \ddot{\boldsymbol{\varphi}}_h \cdot \delta\boldsymbol{\varphi}_h + \mathbf{P}_h : \nabla_0 \delta\boldsymbol{\varphi}_h) dV - \sum_e \int_{\partial_I \Omega_0^e} \mathbf{N} \cdot \mathbf{P}_h \cdot \delta\boldsymbol{\varphi}_h dS$$

$$= \sum_e \int_{\partial_N \Omega_0^e} \bar{\boldsymbol{T}} \cdot \delta\boldsymbol{\varphi}_h dS + \sum_e \int_{\Omega_0^e} \rho_0 \boldsymbol{B} \cdot \delta\boldsymbol{\varphi}_h dV \quad \forall \delta\boldsymbol{\varphi}_h \in X_{hc}^k \quad \forall t \in T \qquad (3.10)$$

The term on the interior boundary $\partial_I \Omega_0^e$ may include fields that are discontinuous and therefore can have different values on either side of a surface. This is a defining characteristic of DG methods which address this problem with the concept of numerical flux. A full description of numerical flux is given in the work by Noels and Radovitzky [23]. Including numerical flux in Equation (3.9), the weak formulation simplifies to Equation (3.11) where the jump $,[\![\partial \bullet]\!] = \bullet^+ - \bullet^-$, and mean $,\langle \bullet \rangle = \frac{1}{2}[\bullet^+ + \bullet^-]$, operators are defined on the space of the trace of functions which can adopt multiple values on the interior boundary.

$$\int_{\Omega_0^e} (\rho_0 \ddot{\boldsymbol{\varphi}}_h \cdot \delta\boldsymbol{\varphi}_h + \mathbf{P}_h : \nabla_0 \delta\boldsymbol{\varphi}_h) dV - \int_{\partial_I \Omega_0^e} [\![\delta\boldsymbol{\varphi}_h]\!] \cdot \langle \boldsymbol{P}_h \rangle \cdot \boldsymbol{N}^- dS$$

$$= \int_{\partial_N \Omega_0^e} \bar{\boldsymbol{T}} \cdot \delta\boldsymbol{\varphi}_h dS + \int_{\Omega_0^e} \rho_0 \boldsymbol{B} \cdot \delta\boldsymbol{\varphi}_h dV \quad \forall \delta\boldsymbol{\varphi}_h \in X_{hc}^k \quad \forall t \in T \qquad (3.11)$$

In Equation (3.11), it is assumed that the constitutive law is enforced strongly from the compatible deformation gradient, $\boldsymbol{F}_h = \nabla_0 \boldsymbol{\varphi}_h$. Also, the displacement compability must be weakly enforced aiding in numerical stability. To do this, a quadratic stabilization term in $[\![\boldsymbol{\varphi}_b]\!]$, $[\![\delta\boldsymbol{\varphi}_b]\!]$ is used. For non-linear mechanics, the terms must be proportional to $[\![\delta\boldsymbol{\varphi}_h]\!] \otimes \mathbf{N}^- : \mathbb{C} : [\![\boldsymbol{\varphi}_h]\!] \otimes \mathbf{N}^-$ where $\mathbb{C}$ is the tangent moduli of the material. Using this term, the displacement jumps are stabilized in the numerical solution, and the material relations at large displacements are considered. The final formulation consists of finding $\boldsymbol{\varphi}_h \in X_h^k$ such that Equation (3.12) holds where h_s is the element size and $\beta > 0$ is the stabilization parameter.

$$\int_{B_{0h}} \rho_0 \ddot{\boldsymbol{\varphi}}_h \cdot \delta\boldsymbol{\varphi}_h + \mathbf{P}_h : \nabla_0 \delta\boldsymbol{\varphi}_h dV + \int_{\partial_I B_{0h}} [\![\delta\boldsymbol{\varphi}_h]\!] \cdot \langle \boldsymbol{P}_h \rangle \cdot \mathbf{N}^- dS$$

$$+ \int_{\partial_I B_{0h}} [\![\delta\boldsymbol{\varphi}_h]\!] \otimes \mathbf{N}^- : \langle \tfrac{\beta}{h_s} \mathbb{C} \rangle : [\![\boldsymbol{\varphi}_h]\!] \otimes \mathbf{N}^- dS$$

$$= \int_{B_{0h}} \rho_0 \boldsymbol{B} \cdot \delta\boldsymbol{\varphi}_h dV + \int_{\partial_N B_{0h}} \delta\boldsymbol{\varphi}_h \cdot \bar{\boldsymbol{T}} dS \quad \forall \delta\boldsymbol{\varphi}_h \in X_{hc}^k \quad \forall t \in T \qquad (3.12)$$

3.3.2 Cohesive Zone Model

For simulation the lose of material strength during fracture, a cohesive zone model is utilized. A cohesive zone model for fracture is based off the idea of considering fracture as a process of separation in material close to the tip of a forming crack [15]. In order to model the gradual decline in the strength of a material as the elements separate a Traction Separation Law (TSL) is used. The formulation used within SUMMIT and for this project is an extrinsic approach with a linear irreversible softening law [15, 24, 25]. This model works well for materials that exhibit initially rigid response along the fracture surfaces. Due to the low strain failure of the Dyneema, as well as the brittle behavior of the matrix material, the extrinsic approach is reasonable for the application. The linear irreversible softening law is one of the most widely-used extrinsic cohesive laws and was originally proposed by Camacho and Ortiz [25]. The formulation of this approach is summarized below based off the formulation in Seagraves and Radovtizky work [15] and is tested using a bar spall simulation.

Formulation

The cohesive zone model is based on the use of the TSL. The TSL becomes active when the criterion in Equation (3.13) is satisfied where σ_n and σ_t are the normal and tangential stress, respectively, β represents the ratio of G_{IIc}/G_{Ic}, and σ_c is the critical effective cohesive strength.

$$\sigma_c \leq \sqrt{\sigma_n^2 + \frac{1}{\beta}\sigma_t^2} \tag{3.13}$$

Once the traction separation law is initiated, the effective separation δ in Equation (3.14), is used to determine the effective cohesive traction, Equation (3.15). In Equation (3.14), Δ_n and Δ_t are normal and tangential component of the separation.

$$\delta = \sqrt{\beta^2 \Delta_t^2 + \Delta_n^2} \tag{3.14}$$

$$T = \frac{\partial \phi(\delta, \boldsymbol{q})}{\partial \delta} \tag{3.15}$$

In Equation (3.15), $\phi(\delta, \boldsymbol{q})$ is the free energy density. For the particular case of the linear irreversible softening law, the effective cohesive traction is given by Equation (3.16) where
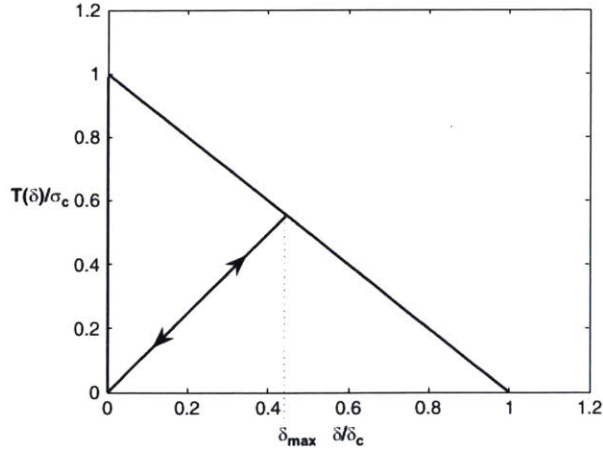
Figure 3-1: T-δ relationship for the linear decreasing extrinsic law [15]

δ_{max} is the largest separation the crack experiences before closure or the current size of the crack as it grows. In Equation (3.16), δ_c is the separation where complete decohesion ($T \equiv 0$) occurs and T_{max} is the effective traction at $\delta = \delta_{max}$. Figure 3-1 depicts the relationship between T and δ as the traction separation law progresses based off Equation (3.16).

$$T(\delta, \delta_{max}) = \begin{cases} \sigma_c\left(1 - \frac{\delta}{\delta_c}\right) & \text{for} \quad \dot{\delta} \geq 0, \delta = \delta_{max} \\ \\ \frac{T_{max}}{\delta_{max}}\delta & \text{for} \quad \dot{\delta} < 0, \text{ or } \delta < \delta_{max} \end{cases} \tag{3.16}$$

The total work of separation for the linear softening law is:

$$\phi_{sep} = \frac{1}{2}\sigma_c\delta_c \tag{3.17}$$

which is directly related to the Griffith critical energy release rate.

Bar Spall Test

The cohesive zone model shown above was tested with a simple bar spall test. The bar spall test was utilized in the work by Radovitzky et al. [24] to validate the discontinuous Galerkin and cohesive element behavior. This spall test was implemented in SUMMIT to confirm no errors existed in the prior implementation of the cohesive zone model. The bar spall consists of a rod of Neohookean material subjected to a tensile wave created by applying a normal
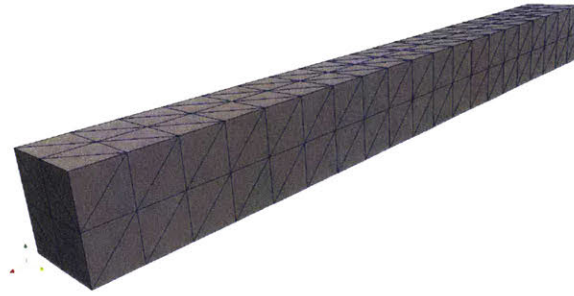
Figure 3-2: Structured 3D Mesh for Bar Spall test with 480 elements

velocity at each end of the bar. For the bar spall test shown here, the velocity on the ends of the rod is $6.046\,\mathrm{m\,s^{-1}}$. The Neohookean material is defined by a Young's Modulus of $260\,\mathrm{GPa}$ and a Poisson's Ratio of 0 with a density of $3690\,\mathrm{kg/m^3}$. The necessary cohesive parameters are the Griffith critical energy release rate and the critical stress from which the critical separation can be calculated using Equation (3.17). The Griffith critical energy release rate is $34\,\mathrm{J/m^2}$ and the critical stress is $360\,\mathrm{MPa}$ giving a critical separation of $0.188\,\mathrm{\mu m}$.

Using the above material parameters, the bar spall simulation is set up using the mesh shown in Figure 3-2. Applying the velocity to each end, the tension wave propagates to the center then the two waves combine, making a stress high enough to create fracture as can be seen in Figure 3-3b. The displacement also becomes constant in the two halves as the separation has occurred as seen in Figure3-3a. Based off the results of the bar spall test, the implementation is correct and verified.

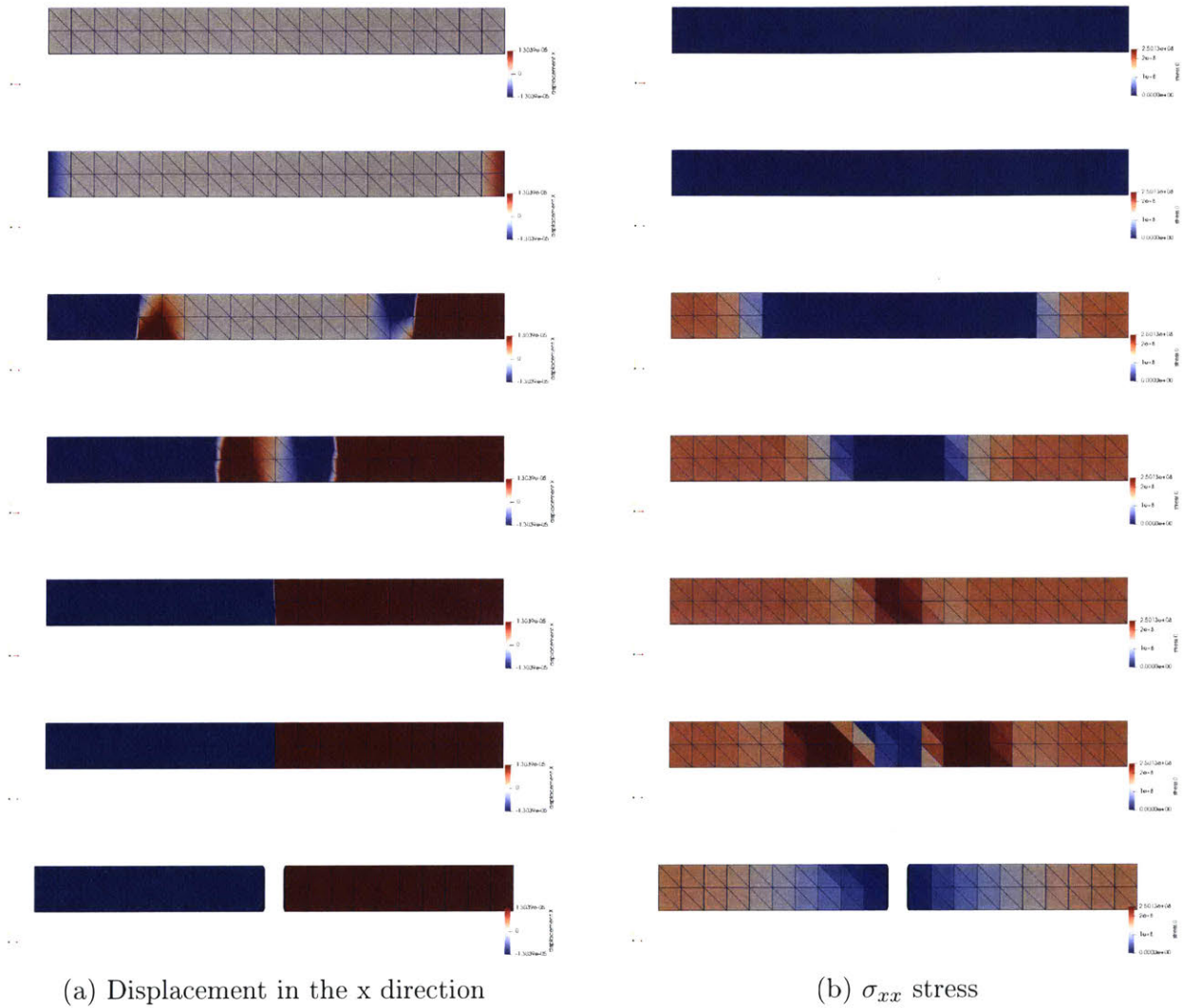(a) Displacement in the x direction   (b) σ_{xx} stress

Figure 3-3: Left: X-displacement as the velocity is applied at the time, velocity progresses toward the center of bar until frac occurs then both sides separate. Right: Stress in the x-direction shows a wave propagate towards the center, create fracture and then reflect until it dissipates. The final images have increased displacement to illustrate successful fracture.

THIS PAGE INTENTIONALLY LEFT BLANK

Chapter 4

Model Calibration and Results

Using the material constitutive models for the Roma Plastilina clay and the Dyneema plate, discussed in Chapter 2 and Appendix A, respectively, the experimental tests are simulated and the material models are calibrated to obtain results that are within the desired range of the experimental tests. There are three tests that are used to calibrate the material. The first is a drop test which is characterized as a low strain rate test. This experiment is originally used to make sure that the clay is conditioned properly prior to high-velocity impact tests and has set bounded that determine if the clay is conditioned properly or not. This test is discussed in Section 4.1 and is used to help provide more information about the clay behavior under an impact. Using the parameters obtained from the drop test experiment, the next two tests are both high strain rate simulations as they involve high-velocity projectiles. The first test is a high-velocity impact with a 9mm projectile and the second is an unknown projectile called Threat M. The tests and material calibration for these two threats are discussed in Section 4.2. The high-velocity projectile tests have a slight added complexity as there is an plate plate on top of the plate which absorbed the majority of the impact from the projectiles. To reduce the number of variables in the calibration, a set of Dyneema parameters were selected as discussed in Section 4.2.2.

To determine a starting point for the material calibration, literature on the characterization of Roma Plastilina or modeling clay was used [9, 8, 6, 5, 7]. The work by Hernandez focused on low strain rates associated with drop test experiments [6, 5, 7]. Hernandez's work on clay did not have a large range of strain rates, but the work from Buchely offered the
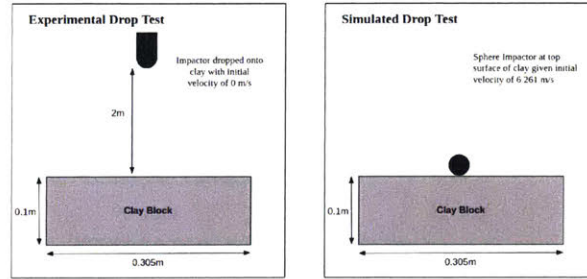
41

Figure 4-1: Left: Experimental Drop Test set up with impactor dropped from 2 m, Right: Simulation Drop Test set up with sphere impactor positioned at top surface of clay and given a kinetic energy equal to the potential energy at 2 m

largest range of strain rates (2300/s to 17,900/s) [8]. Buchely provided information about how the material parameters may change at higher strain rates. For the Young's Modulus, a range of 1.73 MPa to 11.64 MPa was observed for the Roma Plastilina while the yield stress was between 0.08 MPa and 0.153 MPa and the Poisson's ratio was observed at 0.43 [8]. Based on the goal of finding a single parameter set for the clay material, in this work, the ranges of parameters from literature were used as a starting point. However, with different model formulations, the material parameters proposed by Buchely were slightly deviated from the values when calibrating in SUMMIT. The following sections discuss the process of obtaining one parameter set for a variety of impacts.

## 4.1 Low Strain Rate - Drop Test Simulations

4.1.1 Mesh and Impactor

The drop test simulation is used to calibrate the clay parameters. The drop test, used by the Army Research Laboratory (ARL) for verifying the clay is well conditioned for high-velocity impact experiments, consists of a clay block 0.305 m wide by 0.305 m long by 0.1 m high, impacted with a 1 kg impactor [26]. The impactor is a cylinder with a hemisphere on the end impacting the top surface of the clay after being dropped from a height of two meters as shown in Figure 4-1.

To simulate the ARL drop test configuration, the setup is modified to reduce computational time and impactor complexity. The simulated drop test uses a clay block with
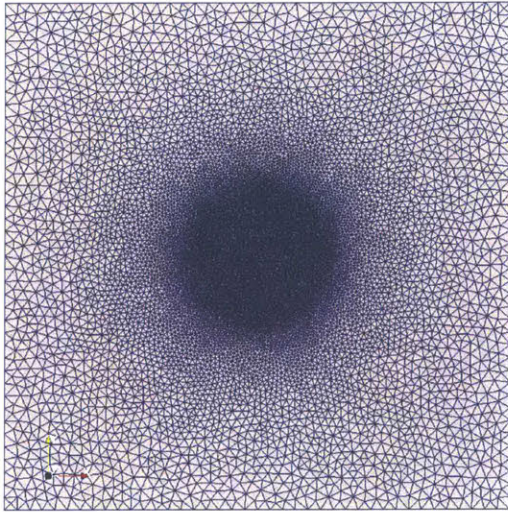
(a) Top view of Clay Mesh
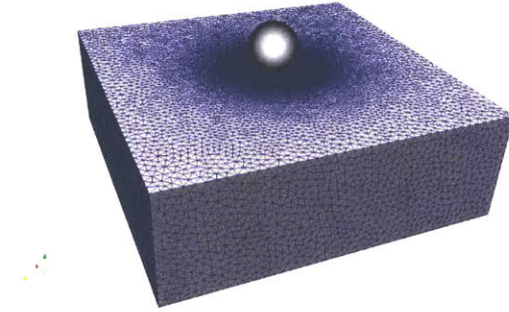
(b) Angled view of Clay Mesh with impactor

Figure 4-2: Clay mesh for the drop test simulation, includes a clay box $0.305\,\text{m}$ wide by $0.305\,\text{m}$ long by $0.1\,\text{m}$ high which consists of 263,000 tetrahedral elements

the same dimensions as the experimental clay block, however the simulation impactor is positioned on the surface of the clay. At this point, the simulation impactor is given a velocity based on the initial potential energy the impactor had at $2\,\text{m}$ which corresponds to $6.261\,\text{m}\,\text{s}^{-1}$. The impactor is modeled as a sphere due to the contact algorithm discussed in Appendix B. A mesh of the impactor is not needed as the radius of $0.0225\,\text{m}$ can be set as the contact radius. Using the contact algorithm, the impactor is a single point representing the sphere impactor. The upper cylindrical portion of the experimental impactor is ignored but is considered acceptable as discussed in Fronk's prior work [11].

The mesh for the drop test simulation is shown in Figure 4-2. The mesh contains approximately 263,000 tetrahedral elements. The mesh is refined at the impact point to accurately capture the clay response. During the impact the elements experience high distortion and using smaller elements helps to mitigate the numerical instabilities leading to mesh refinement at the impact point [11]. The outer region is not refined since there is little deformation or mesh distortion and has minimal impact on the clay indentation. The drop test simulations are run using continuous Galerkin elements preventing fracture or separation of elements.

Parameter Set	$E(MPa)$	μ	$p_0(MPa)$	m	α	$\dot{\epsilon}_0^p$	Depth (mm)
1	20	0.4	1	2	10	100	26.8
2	20	0.4	1	2	13	200	26.6
3	20	0.4	1	2	15	300	26.0
4	15	0.4	1	2	10	100	27.3
5	20	0.4	1	30	20	100	26.4
6	20	0.4	1	5	15	100	26.2
7	20	0.4	0.1	2	35	100	25.1
8	5	0.4	1	2	12	100	26.1

Table 4.1: Cam-clay Parameter Sets that produce clay indentation with range of calibration for experimental drop tests with $\rho = 1529 \ kg/m^3$, $V_{ref} = 0.75$. The experimental drop test depth is 25.4 ± 2.5 mm

4.1.2   Results

In order for the drop test results to be deemed calibrated, the depth of the impact must be within the acceptable bounds of clay indentation between 22.9 mm and 27.9 mm as specified by ARL. A clay specimen with an indentation depth measured within the acceptable bounds is considered well-conditioned and can be used for the high-velocity impact experiments.

A variety of parameter sets that produce a clay indentation within the experimental range mentioned above are determined. The parameter sets are shown in Table 4.1. Multiple parameter sets are used to allow for further refinement at higher strain rates (Section 4.2). In the Table 4.1 it is seen that a wide variety of parameters can produce the depth required to meet the ARL clay calibration criteria. Although only eight parameter sets are shown, roughly 70 different parameter sets were found which also fit within the range specified. The results shown here are a sampling of those parameter sets but focus on the parameter sets that will be shown in Sections 4.2 and 4.3.

In Figure 4-3, the final time step of the eight parameter sets of Table 4.1 are shown. Based on the images, the impactors enters the clay and pushes the clay to the side creating a bulge outside the impact point. Depending on the parameters, the bulge is more or less pronounced. As seen in Figure 4-3g a high internal friction angle reduces the build up of material around the impactor. The high internal friction angle increased the friction within the material preventing it from sliding leading to reduced bulging. It can also be seen in Figure 4-3e, that a high rate sensitivity exponent will lead a large amount of build up along the edge of the impact region. Based on the power law rate-sensitivity discussed in Section 2.2, a high rate sensitivity exponent lessens the rate dependence producing a constant stress

Parameter	Effect of decreasing parameter
Young's Modulus	Increase
Preconsolidation Pressure	Increase
Rate Sensitivity Exponent	Decrease
Internal Friction Angle	Increase
Reference Plastic Strain Rate	Decrease

Table 4.2: Effect of varying parameters on final clay indentation

after yield. The constant stress allows for higher strains leading to more build up of material. The bulging up of clay is also seen in the experimental drop test so the resulting shape of the simulation qualitatively matches the experiments.

Based of the results of the various tests run, the effect each parameter has on the final depth of the clay can be determined in order to help guide further calibration for higher or lower strain rates. Table 4.2 reflects the effect each parameter has on the final indentation in the clay when independently decreased. When increasing each parameter independently the opposite affect is seen thus not shown in Table 4.2. Some of the observations can be checked by comparing against understanding of the parameter meaning while others are less intuitive and thus offer more insight into the material behavior. For example, increased indentation for decreased elastic modulus. However, it was not initially clear how the preconsolidation pressure, rate sensitivity exponent, internal friction angle, and reference plastic strain rate affected the indentation as they were manipulated. But, from the results of the various simulations the relations shown in Table 4.2 serve as guides to obtain desired indentation depths for various parameter sets.

4.2 High Strain Rate - High-velocity Impact Simulations

4.2.1 Mesh and Impactors

The high-velocity impact simulations are set up differently than the drop test since there is a smaller impactor moving at a higher speed with a plate of plate over the clay. The clay is used to measure the maximum back-face deformation of the Dyneema plate. Figure 4-4 shows the mesh primarily used for the impact simulations. The mesh contains 41,000 linear
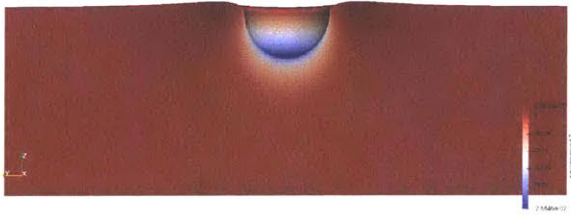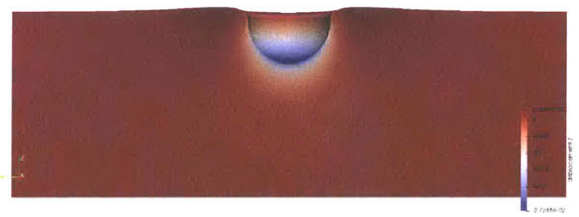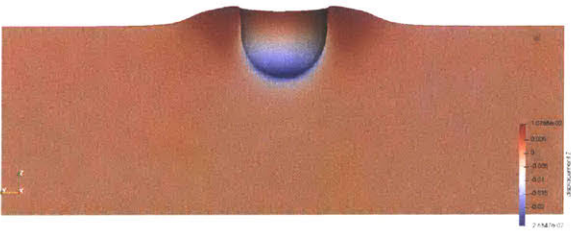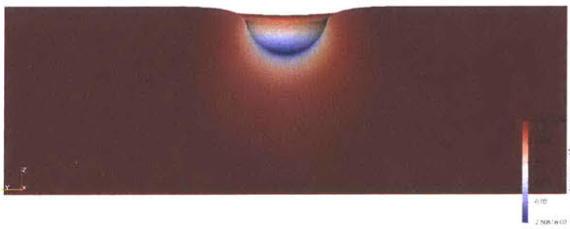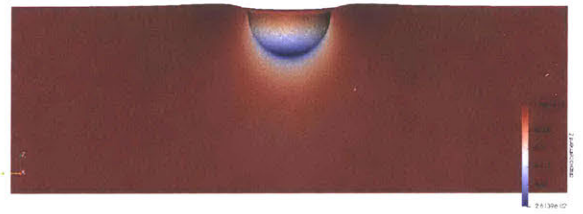
(a) Set 1
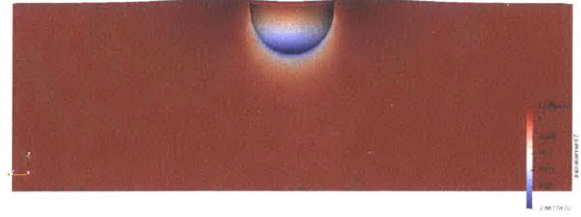
(b) Set 2
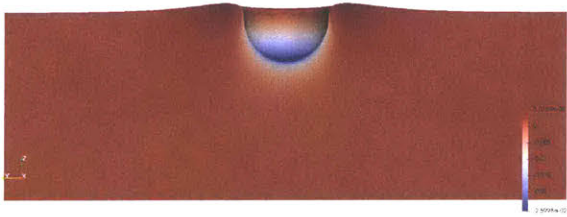
(c) Set 3

(d) Set 4

(e) Set 5

(f) Set 6

(g) Set 7

(h) Set 8

Figure 4-3: Clay shape for eight clay parameters sets that are valid options and hold to criteria for experimental tests

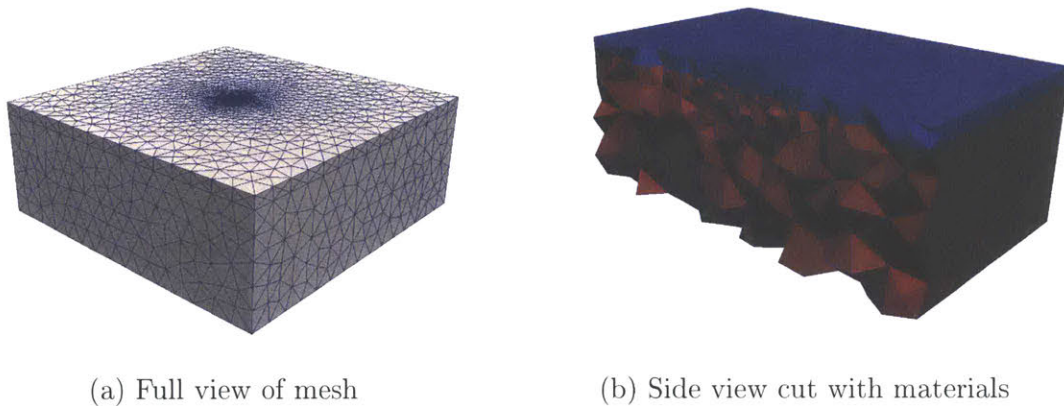(a) Full view of mesh   (b) Side view cut with materials

Figure 4-4: The clay and plate system has 41,000 tetrahedral elements with local refinement around the point of impact. The blue material indicates Dyneema while the red material indicates Roma Plastilina Clay.

tetrahedral elements and includes mesh refinement at the impact point. The mesh contains two materials. The first is the thin Dyneema plate and the second is the block of Roma Plastilina clay on the bottom. The Dyneema plate has a width of 0.3m, length of 0.3 m and height of 0.011m. The clay has the same width and length but has a height of 0.089 m as specified by the experimental configuration. The plate mesh is refined in a cylinder region that is slightly larger than the 9mm impact in order to include edge effects from the impact. This refinement continues down into the clay where the top face of the clay has the same refinement. The mesh is not refined on the boundaries, as these regions do not encounter large distortion and no localized refinement is needed.

There are two high-velocity projectiles considered, 9mm and Threat M. The 9mm models a 9mm bullet and has an impact velocity of 427 m/s. The Threat M, on the other hand, is a smaller bullet having an impact velocity of approximately 743 m/s. Both impactors are modeled using a sphere similar to that used in the drop test experiments. For the 9mm bullet the sphere has a radius of 0.0045 m, while the Threat M has an approximate radius of 0.00391 m. Although the spherical shape does not match the shape of standard bullets, the sphere impactor is transferring energy into the plate the same way the bullet would so without adding complexity of the bullet getting damaged, thus results that are in the desired range were produced.

To get an accurate result with the clay, the high-velocity impact simulations are tested
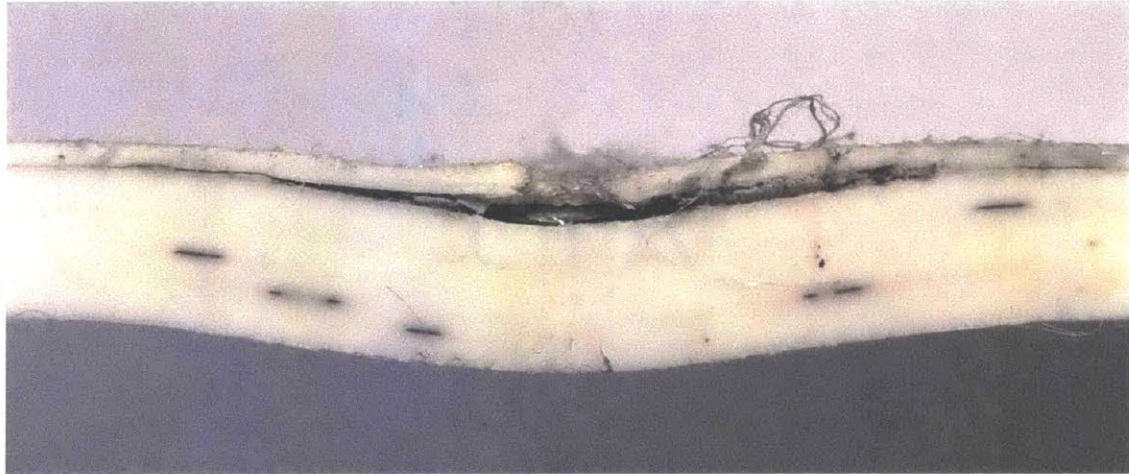
Figure 4-5: Cross-section of the plate cut through the center after impact from 9mm threat

and calibrated to ensure that the results are within the expected range to fully define the clay. The parameter sets from the drop test experiments are used as a starting point to determine the best set of parameters for the high strain rate simulations. Having a variety of options and an understanding how the material parameters shape the indentation (shown in Table 4.2, helps to calibrate the clay to work for both the low strain rate and high strain rate simulations.

Plate Configuration

Prior to modeling the plate as a single layer of material as shown in 4-4, the Dyneema plate was tested in various configurations to determine how best to successfully model the physical behavior of the material in the experiments. From the samples provided by ARL, the plate appears to have penetration through several layers on the top face and there is delamination between the penetrated layers and the rest of the plate as seen in Figure 4-5.

To model the penetration and then delamination of the Dyneema, a few different configurations were tested which integrated varying meshes and use of the cohesive zone model. The first configuration tested involved placing a cylinder the width of the projectile at the impact point and making the plate two layers as shown in Figure 4-6a. This configuration allowed for penetration into the material by forcing fracture paths along the vertical that was approximately the width of the projectile as shown in Figure 4-6b. From the impact simulation it is clear that the configuration in Figure 4-6a produces the fracture seen in

48

(a) Cylinder at impact point and plate in two layers

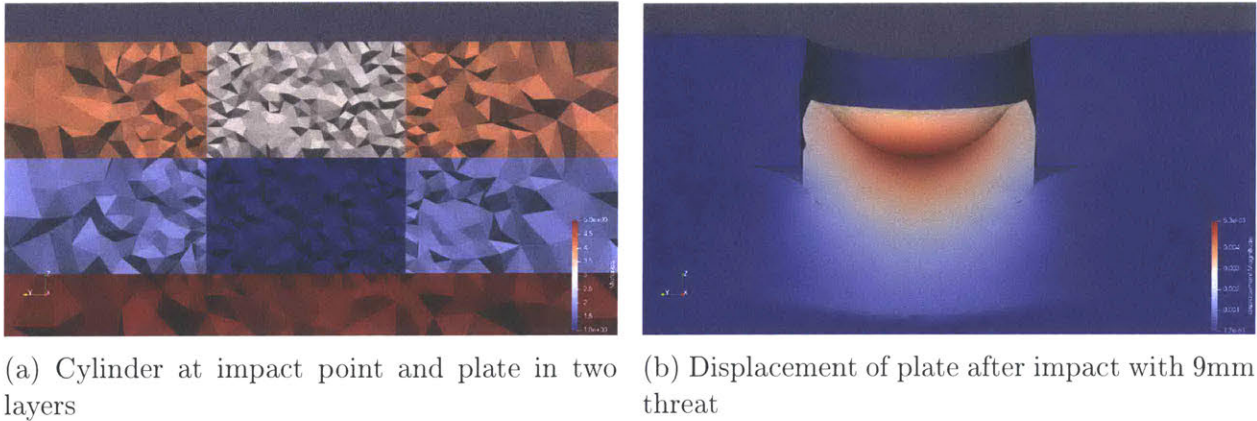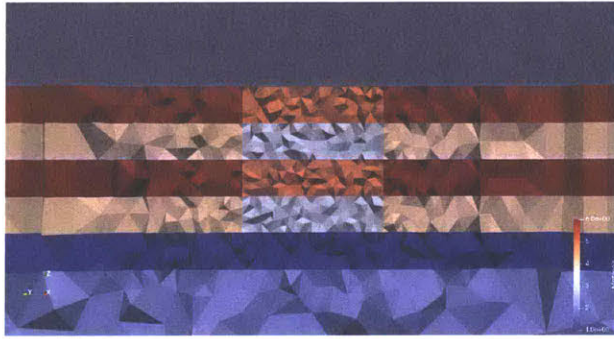(b) Displacement of plate after impact with 9mm threat

Figure 4-6: Dyneema plate configuration with two layers and a cylinder that puts a fracture path on the vertical

the experiments, but that the two layers of resolution was not enough to have delamination occur in the area desired. Additionally, if the vertical cohesive strength was too low, then the whole cylinder would displace and fully separate and the clay would only be impacted by the cylinder of material.

The problems with the two layer configuration led to a Dyneema configuration in which a cylinder was still used, but the Dyneema was separated into 5 layers to offer more freedom in the delamination point of the plate. In Figure 4-7a, the mesh is shown of the five layer configuration in which the first four layers have the cylinder added, but the last layer is continuous to prevent full separation of the cylinder from the rest of the plate. This configuration was implemented to allow for control in the penetration depth for the plate but led to fracture that was all along the cylinder and then a inaccurate back-face shape was created from the cylinder impacting the continuous layer at the bottom of the plate. There was delamination within the regions desired, but the large vertical fracture paths posed problems in producing adequate shaping on the backface of the plate. Additionally, the imposed vertical fracture paths are not allowing the material to fracture where it may actual fracture in the experiments.

To mitigate the problems from the imposed vertical fracture paths, an eight layer configuration without imposed vertical fracture paths was implemented to allow vertical fracture to occur naturally. The shift from five layers to eight layers was done to give more resolution to the material and to produce layers that are approximately one element thick to aid in
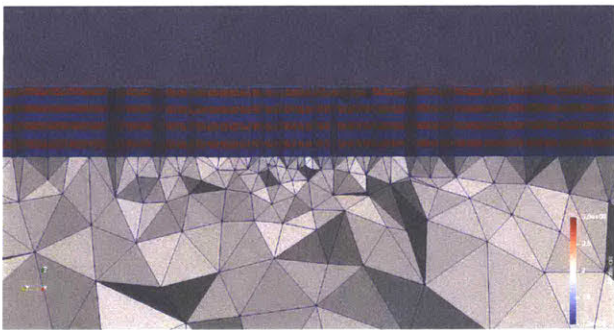
(a) Cylinder at impact point and plate in five layers with a continuous bottom layer
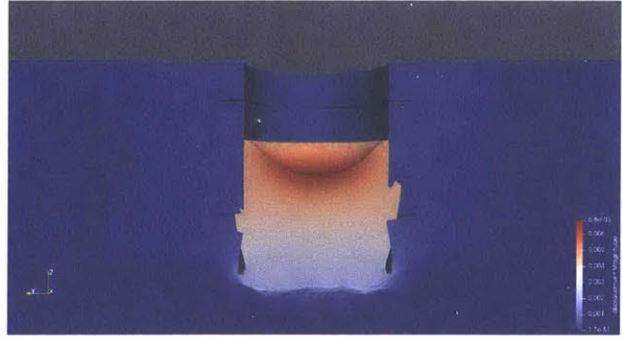
(b) Displacement of plate after impact with 9mm threat

Figure 4-7: Dyneema plate configuration with 5 layers and a cylinder that puts a fracture path on the vertical

(a) Dyneema plate in eight layers with all continuous layers
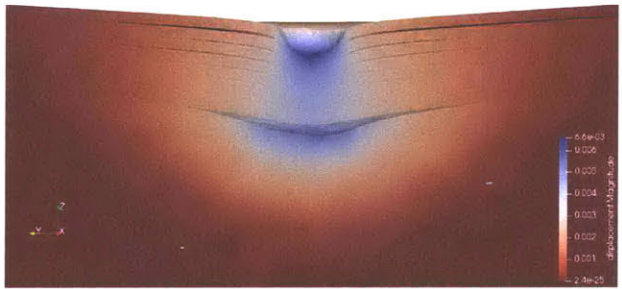
(b) Displacement of plate after impact with 9mm threat

Figure 4-8: Dyneema plate configuration with five layers and a cylinder that puts a fracture path on the vertical

the vertical shearing seen in the experiments. The mesh shown in Figure 4-8a shows the eight layers and Figure 4-8b shows the displacement of the plate after the impact from the 9mm projectile. This configuration produced the delamination in a similar manner as seen in the experimental results. Although the delamination occurred, the vertical fracture did not occur at the edges of the impactor, but rather below the impact where the stress is higher. This prevented the shearing of the material as the stress was released in the middle of the layer, which minimized the stress at the impact edges. In an attempt to see more vertical fracture, the cohesive strength was lowered, but this produced instabilities in the material that led to failure of the simulation.

ρ	$E(GPa)$	ν	$\sigma_y(MPa)$	ε_0^p	$\dot{\varepsilon}_0^p$	m	n
1026	25	0.15	100	3.5e-3	1.4e2	1	10

Table 4.3: Dyneema Parameter Set used for high-velocity impact simulations

After testing the various configurations of the Dyneema plate, it was decided that the best and simplest way to model the plate was using a single layer of material that produced a final back-face shape that matched the back-face shape of the experiments. Although the delamination is not included in this model, the energy absorbed by the delamination is assumed small and did not lead to large differences in the final results. For the vertical fracture, in order to simulate this without using explicit fracture, the Dyneema material needs to be softer than standard material models indicate to allow for more plasticity. The increased plasticity will allow for more energy absorption which is the result of the fracture.

4.2.2 Dyneema Parameters

For the high-velocity impact simulations, the Dyneema parameters used are shown in Table 4.3 with the variables described in Appendix A. These parameters were determined using the experimental plates along side the simulations. The experimental plates have a permanent back-face shape and when the simulations are completed, the plate also creates a back-face permanent deformation shape. The parameter set used for the simulation was generated by comparing the two final back-face shapes and proposed material parameters from literature [12, 27, 28, 29, 30]. This parameter set may be slightly different compared to true Dyneema due to the lack of penetration and the use of a single layer in the simulated plate.

4.2.3 9mm Threat

The simulation results using an optimized material parameter set (Table 4.4) are shown in Figure 4-9. There are three material parameter sets shown. Each set produces slightly different results in the depth as seen in Table 4.4 and will be discussed below.

It can be seen that by increasing the internal angle of friction and the reference plastic strain rate, the shape of the clay deformation changes. With the higher angle, the deformation of the clay becomes more of a hole as opposed to a smooth indentation. The

51

Parameter Set	$E(MPa)$	μ	$p_0(MPa)$	m	α	$\dot{\epsilon}_0^p$	Depth (mm)
1	20	0.4	1	2	10	100	19.6
2	20	0.4	1	2	13	200	20.4
3	20	0.4	1	2	15	300	20.6

Table 4.4: Cam-clay Parameter Sets for 9mm projectile tests with $\rho - 1529\ kg/m^3$, $V_{ref} - 0.75$. Experimental clay depth is 23.5 ± 0.82 mm for the 9mm projectile.
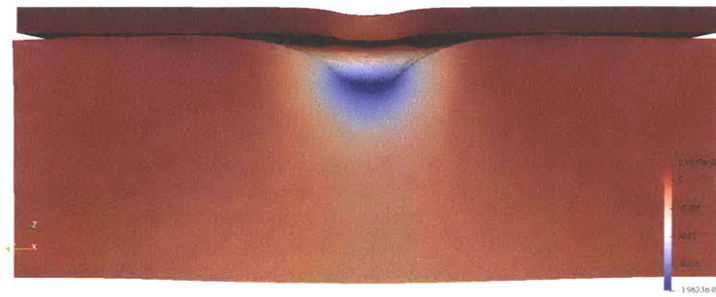
(a) Set 1
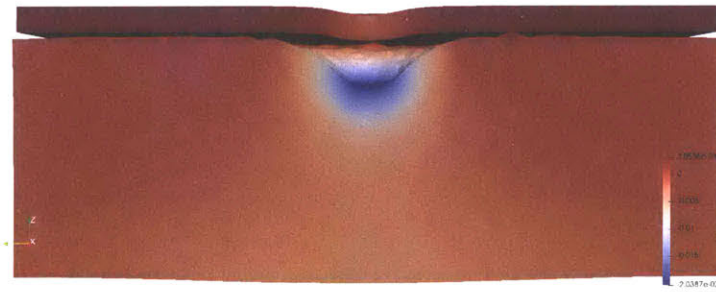
(b) Set 2

(c) Set 3

Figure 4-9: Clay Shape for 9mm high-velocity impact simulations with various parameters sets

Figure 4-10: Comparison between 9mm high-velocity impact simulations and experimental impact simulations for parameter set 3.

experimental results show the shape of the clay after the impact is closer to that of a hole so the parameter sets with a higher angle are more desired. The best parameter set fo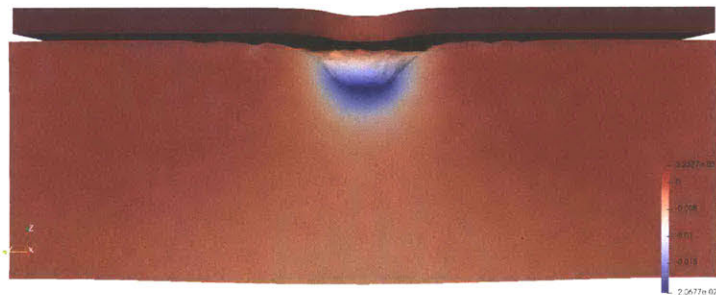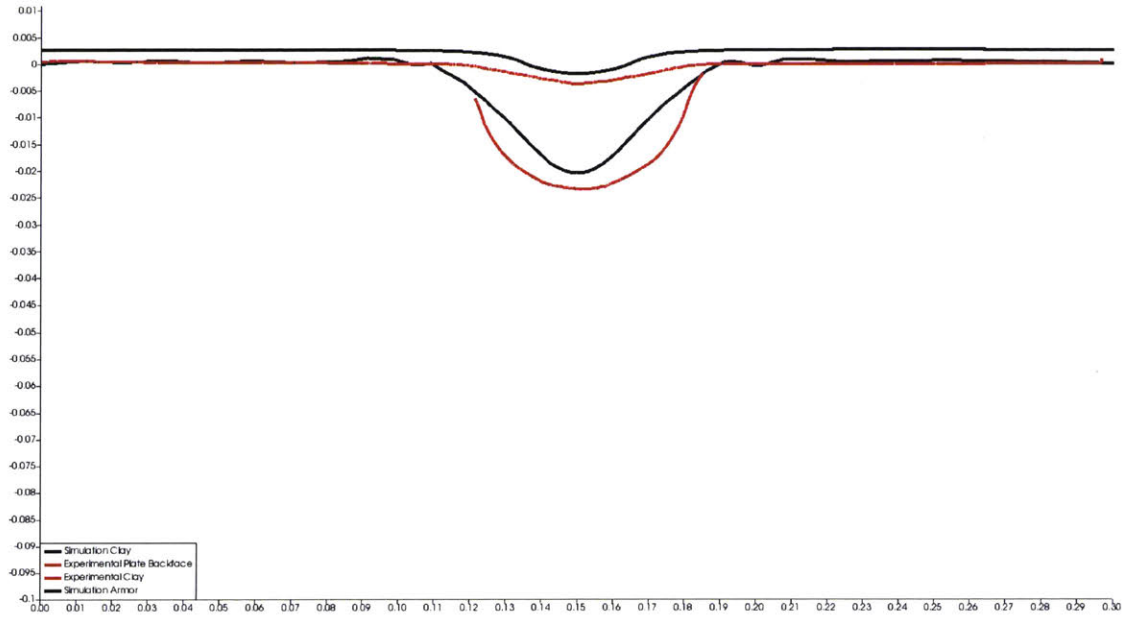r the clay is parameter set 3 where the greatest indentation depth is achieved. From the experimental data, the average depth is 23.5±0.82 mm without the use of pads. The values shown in Table 4.4 are below the average depth from the experimental by about 12%. This difference in the clay indentation depth is a factor of the lack of penetration in the simulated plate thus more energy is being absorbed by the plate than is happening in the experiments. Additionally, there could be more concentration of energy in the experiments due to the penetration and then subsequent deformation of the projectile. However, with the simplified panel, the results are within a reasonable 2 standard deviations of the average result.

The results of the simulated high-velocity impact test can be compared with scans provided by ARL that illustrate the final shape of the clay. Shown in Figure 4-10, the clay shape after impact is over laid the scans of the experimental high-velocity impact experiments. The top lines reflect the final plate shape for both the experiment and the simulations. The simulated plate is higher in the plot than the experimental plate because the simulated plate is allowed to move vertically and after the impact of the high-velocity projectile, it vibrates

53

Parameter Set	$E(MPa)$	μ	$p_0(MPa)$	m	α	$\dot{\epsilon}_0^p$	Depth (mm)
1	20	0.4	1	2	10	100	26.5
2	20	0.4	1	2	13	200	28.0
3	20	0.4	1	2	15	300	28.1

Table 4.5: Cam-clay Parameter Sets for Threat M projectile tests $\rho = 1529\ kg/m^3$, $V_{ref} = 0.75$. Experimental clay depth is 31.6±4.73mm for the Threat M.

and separates from the clay. The simulated clay has a general shape comparable with the experimental result.

4.2.4 Threat M

The Threat M is a smaller impactor (7.8 mm diameter) but is fired at a higher velocity (approximately 743 m/s). With material type, weight and size being unknown due to restricted information, the simulations are estimations based off other high-velocity projectiles that travel around 743 m/s. Using the plate and clay simulation described in Section 4.2.1, the clay deformation created by the impactor is shown in Table 4.5. The results are also visualized in Figure 4-11 to illustrate how the modification of the clay affected the shape of the final clay deformation. In the experiments, the clay depth was 31.6±4.73mm without pads. Based off this average and range, the clay deformation matched is within the desired range for the Threat M. finalparameters

4.2.5 Clay and Plate Separation

Originally, simulations were run with the clay and plate staying in contact throughout the simulation. This was enforced by having a normal continuous Galerkin boundary between the two materials instead of a discontinuous Galerkin boundary. Because the plate was not deforming to the full depth of approximately 23mm, the clay was not reaching the desired depth. To combat this, a contact interface condition is added between the plate and the clay. The contact interface is a variation of the discontinuous Galerkin method described above. Rather than using stress and critical distance to determine separation, the contact algorithm is used. Once the proper plate-clay interface was implemented the plate and clay can separate when the plate stops deforming even though the clay may continue to deform. The contact plate-clay interfaces acts as it would in the experiments since the clay will be
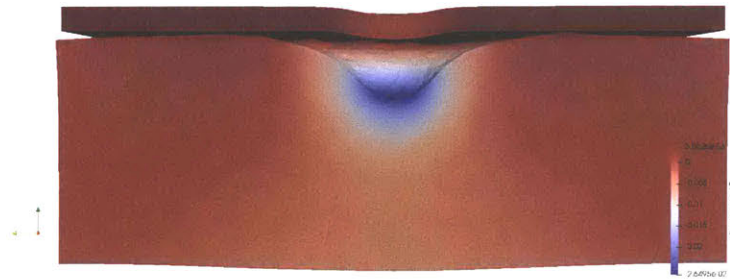
(a) Set 1
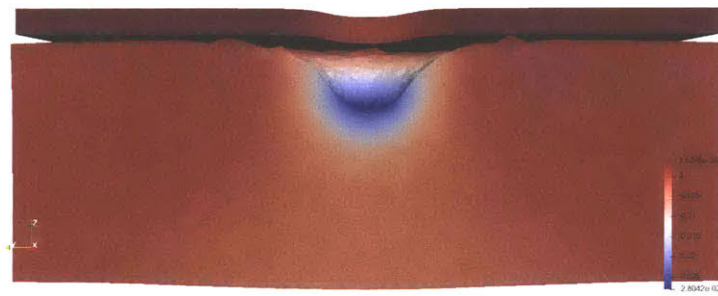
(b) Set 2
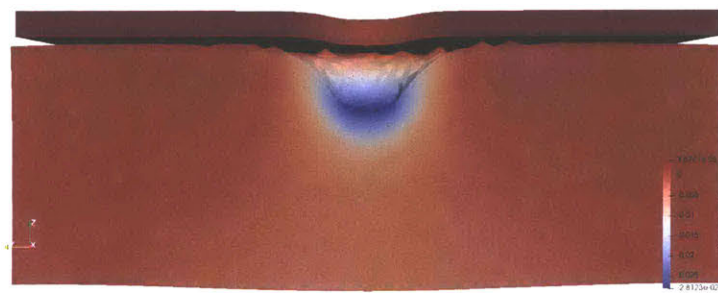
(c) Set 3

Figure 4-11: Clay shape for Threat M high-velocity impact simulations with various parameter sets

Threat Type	Backface Deformation without Pads	Backface Deformation with Pads
9mm	23.5±0.82	0.3±0.06
Threat M	31.6±4.73	16.6±0.35

Table 4.6: Experimental depth of clay after impact with both high-velocity projectiles and two different configurations (with or without padding). The ± gives a range of one standard deviation

in contact with the plate and will not have any force holding the two materials together. This allows the plate and clay to act as two separate materials, as opposed to being forced to move together as would occur in the continuous Galerkin method.

It is seen in high-velocity impact simulations that the clay and plate always separate soon after the impact. The excess energy from the bullet that is not absorbed by the plate is transferred through the plate into the clay. The energy in the clay makes it continue to deform even though the plate has stopped deforming. The clay and plate interaction seen in the simulation goes against what is thought to occur during the experiments. However, based off the physics and strength of the material, the plate cannot deform to the indentation depth of 23mm. Therefore, in order for the clay to indent 23mm, there must be separation and transfer of energy between the clay and plate. This shows that the experiment for the plate and clay is not accurately showing the greatest back-face deformation, but rather the amount of energy transferred into the clay.

This conclusion matches well with the results seen in the simulations when looking at the back-face deformation. As shown in Table 4.6 in impacts without padding, the 9mm bullet creates a clay indentation of approximately 23mm and the Threat M creates a clay indentation of approximately 32mm. With padding, the 9mm creates a clay indentation of approximately 0.3mm while the Threat M still creates an indentation of 16.6mm. For the clay to only show the back face deformation, the change in indentation depth from adding the padding should be similar. However, there is a much larger change in the 9mm case. There is more energy transfer in the Threat M case since it has higher energy leading to a less significant change in the clay indentation.

Parameter Set	$E(MPa)$	μ	$p_0(MPa)$	m	α	$\dot{\epsilon}_0^p$	Depth (mm)
3	20	0.4	1	2	15	300	27.8

Table 4.7: Selected Cam-clay parameter set that produce clay indentation with range of calibration for experimental drop tests and high-velocity impact experiments with $\rho = 1529$ kg/m^3, $V_{ref} = 0.75$

4.3 Final Roma Plastilina Model Parameters

Given the results in the previous sections and the desired range of results from the helmet test experiments, the parameter set 3 is chosen as the best parameter set. This value matches well with the low strain rate and the high strain rate for the Threat M. The set of parameters is slightly off from the value for the 9mm threat due to confounding factors such as the behavior of the projectile or damage in the plate. The parameter set is successfully able to produce accurate results over a wide range of rates which is a point of difficulty for modeling Roma Plastilina.

THIS PAGE INTENTIONALLY LEFT BLANK

Chapter 5

Scalability of SUMMIT

Scalability is used to determine how efficient a simulation is when increasing the number of processors for a particular problem. It is used to determine the best configuration to run a simulation depending on the problem size and the computational resources available. Strong scaling is a case when the problem size is fixed but the number of processors are increased. The goal of a program is to scale linearly meaning the increase in speed is equal to the increase in the number of processors. For example, a simulation is scaled linearly if it takes 20 minutes on 1 processor and it takes 10 minutes on 2 processors. For the scalability done in this work, the ARL Centennial HPC system is used [19]. The Centennial system has 1,784 compute nodes with 40 cores per node which allows for simulations to be run on a large number of processors. An allocated amount of hours is given and in order to effectively use the hours, an optimal number of processors is desired. In the following sections, strong scaling of the drop test and high-velocity impact simulations are shown and discussed.

5.1   Drop Test Simulation

The drop test simulation was run on the ARL Centennial HPC system starting with a fixed problem size then increasing the number of processors. The drop test simulation is compiled from SUMMIT and is using continuous Galerkin. The problem size was then increased by dividing each element into eight individual elements which increased the problem size by a factor of eight. This was repeated three additional times to get five different problem
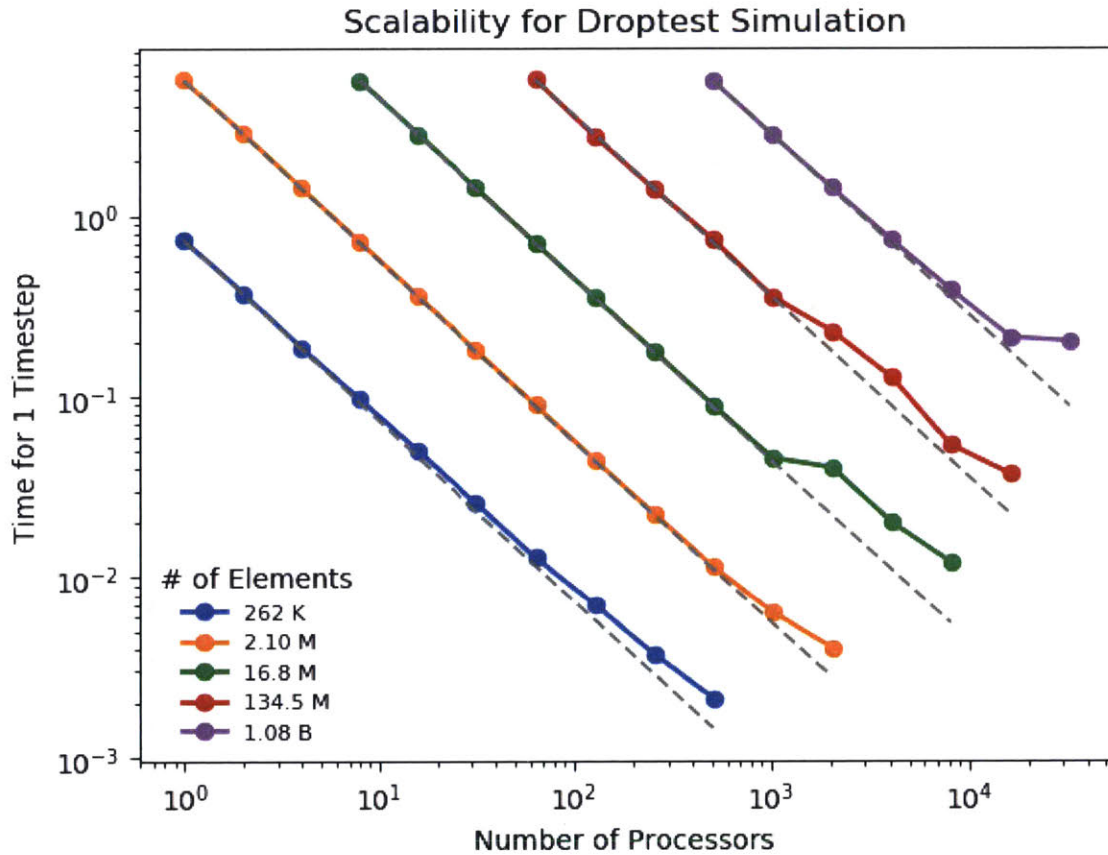
Figure 5-1: Fixed Problem Size scalability for Drop test Simulations (CG, 1st-order tetra-hedrals) on ARL Centennial HPC System (SGI ICE XA - 2.6 PFLOPS)

sizes that are run over an increased number of processors. For the drop test problem, the largest problem size used was 1.08 billion elements and the number of processors increased from 1 to 32,768 by a factor of two. The results are shown in Figure 5-1. The simulation is said to have strong scaling since the scaling curves follow the reference linear scaling. As the number of processors increases, the speed up slowly starts to diverge from the linear line. In order to optimize the simulation, the problem should be run while still on the linear line. Depending on the size of the problem, Figure 5-1 can be used to determine the correct number of processors to use.

Another way to look at the scalability of a program is to fixed the number of elements on a processor. So when the number of elements is increased by a factor of eight, the number of processors also needs to be increased by a factor of eight. The desired result is a flat line as there should be no change in the time needed to solve. Figure 5-2 shows this result for the
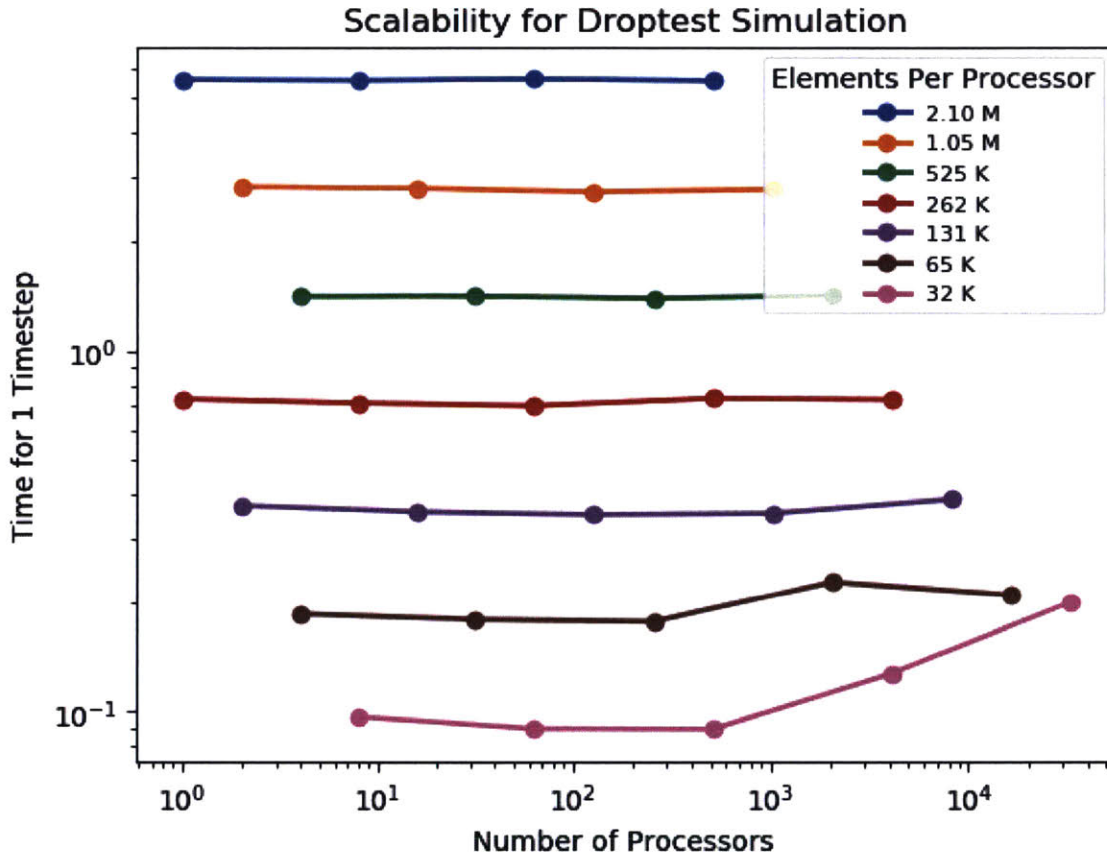
Figure 5-2: Fixed number of Elements per processors scalability for Drop test Simulations (CG, 1st-order tetrahedrals) on ARL Centennial HPC System (SGI ICE XA - 2.6 PFLOPS)

drop test simulation. It can be seen that with less elements per processor, it is not always beneficial to use more processors. For the drop test simulation, the scaling starts to diverge after 256 processors when there are less than 65,000 elements per processor.

For the drop test simulation used, SUMMIT shows strong scaling. The information acquired from the scalability plots above helps to determine how best to optimize the parallelization to effectively use allocated hours. The scaling can also be applied to similar problems that use similar models such as continuous Galerkin first-order elements with a explicit Newmark integrator. The scaling may not significantly change with different materials.

5.2 High-Velocity Impact Simulation

The high-velocity impact simulations have different scaling compared to the drop test simulations since they are done using the discontinuous Galerkin method instead of the continuous Galerkin method increasing the number of degrees of freedom in a problem leading to a higher computational time. A similar process to the one used for the drop test simulations was used for the high-velocity impact simulations. A fixed problem size was used then elements were divided into eight individual elements to create a new problem size that is eight times larger than the first. This was completed two more times to generate four different problem sizes to use for the scalability test. For the high-velocity impact simulations, the largest mesh was 20.7 million elements which is approximately 82.8 million degrees of freedom. For these simulations, due to the smaller size of the mesh, the maximum number of processors used was 4,096. The scalability results of the high-velocity impact simulations utilizing the ARL Centennial HPC System are shown in Figure 5-3. As can be seen, the high-velocity impact simulations have strong scaling for the problem sizes and number of processors tested. The scaling holds to the linear line until starting to slightly diverge from the path. The main difference between this scalability curve and the prior plots is the change from continuous Galerkin to discontinuous Galerkin. Figure 5-3 can be used to determine how best to run the high-velocity impact simulations as well as other simulations that use discontinuous Galerkin first-order tetrahedrals.

Overall, SUMMIT shows strong scaling for both continuous Galerkin and discontinuous Galerkin with first-order tetrahedrals using an explicit newmark solver. 4.
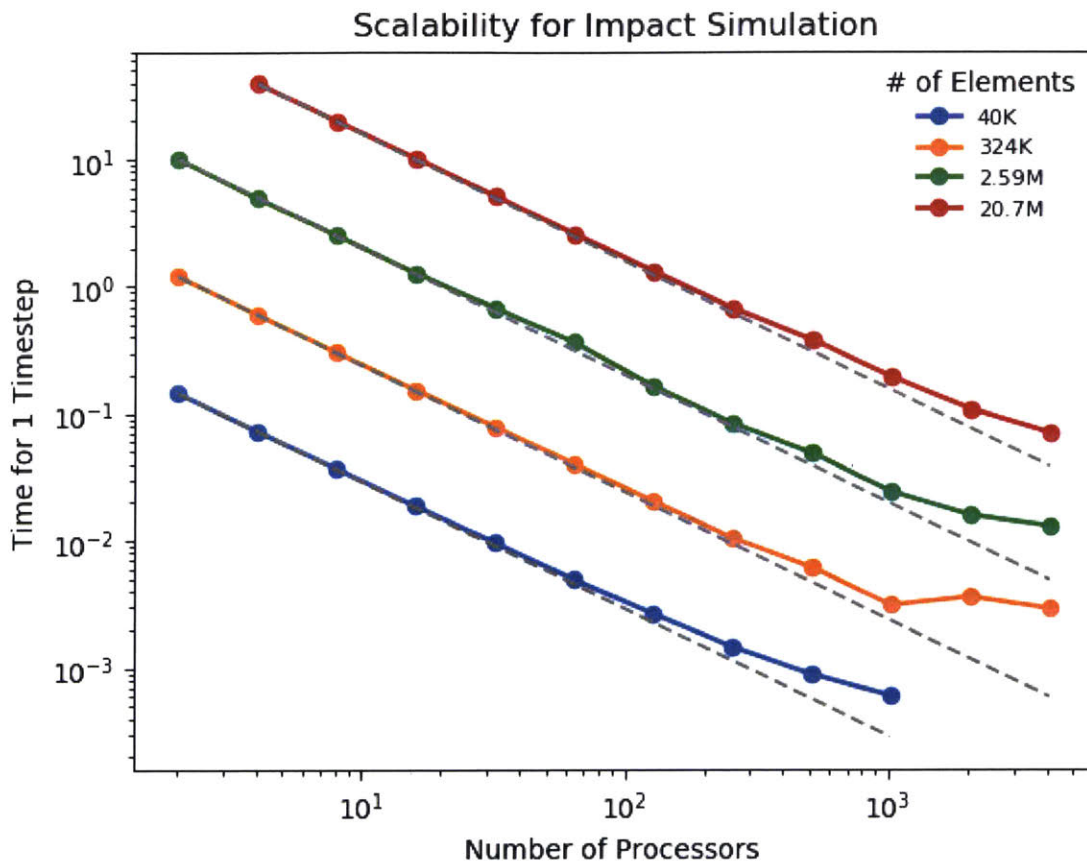
Figure 5-3: Fixed Problem Size Scalability for High-velocity Impact Simulations (DG, 1st-order tetrahedrals) on ARL Centennial HPC System (SGI ICE XA - 2.6 PFLOPS)

THIS PAGE INTENTIONALLY LEFT BLANK

Chapter 6

Application to Fracture of Saturn V Pressurized Tanks

As part of the work with the cohesive zone model, the application of the framework to fragmentation of pressurized tank was explored. For this problem, the goal was to simulate pressurized tank failure in order to determine fragment size and distribution. This project was collaborated on with the Engineering Risk Assessment team at NASA and called for the use of the computational framework discussed in Chapter 3. One benefit of using SUMMIT for this task is the cohesive zone model which allows for mass conservation aiding in the determination of fragment size and distribution. To model the pressurized tank, a single tank size and type was chosen to reduce variables in the problem. The tank chosen is a Helium tank from the Saturn V rocket. The pressurization rate selection process is discussion in the following section and is used for all further full failure problems. In the following sections, the model configuration and loading schemes are discussed and the full tank failure problem is demonstrated.

6.1   Model Configuration and Loading

To model the fracture of an over-pressurized tank, a sphere is used to simplify the geometry. The sphere used has similar dimensions and wall thickness of a Helium tank on the Saturn V rocket made of titanium. The radius is 0.3429 meters with a wall thickness of 0.0084582

(a) SUMMIT Sphere Mesh - Full
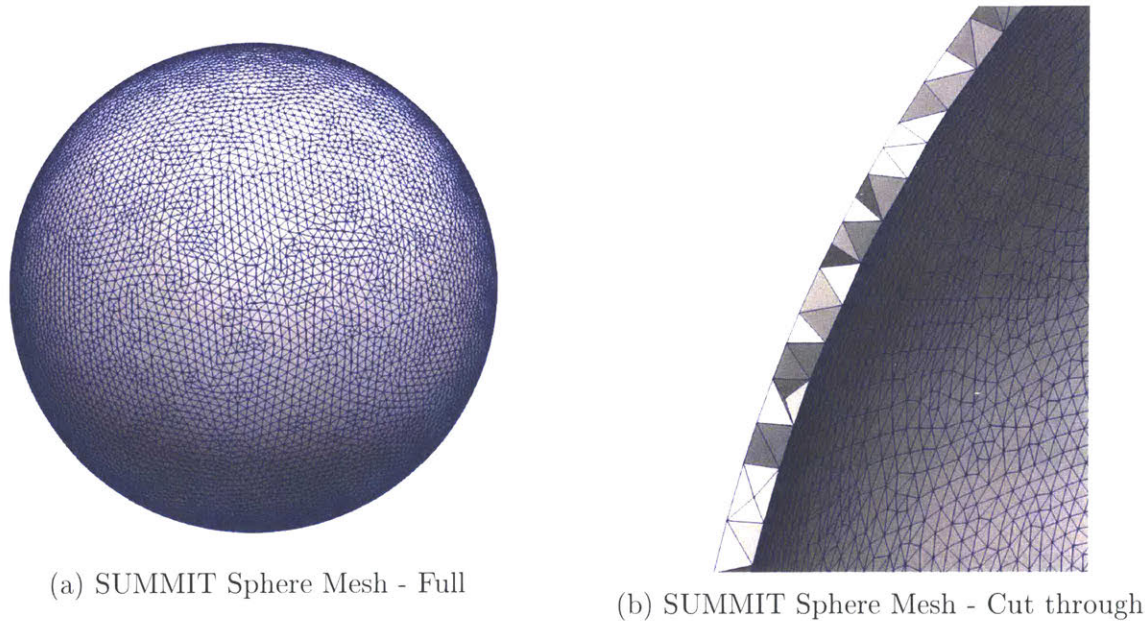

(b) SUMMIT Sphere Mesh - Cut through

Figure 6-1: Sphere meshes for over-pressurization simulations

meters which gives a radius-wall thickness ratio of 40.54:1 [31]. The mesh for the titanium sphere is shown in Figure 6-1a, and a view of a cut through the tank wall in Figure 6-1b to illustrate that although the element size is approximately that of the thickness, there are portions of the mesh which still have two elements through the thickness. The SUMMIT mesh shown consists of 103,621 elements.

Prior to testing the over-pressurization, the pressurization rate is determined. To check the affect of various pressurization rates, the operating pressure of 3000 psi or 20.684 MPa is applied and then held. This results in a ramp up of pressure then a leveling out. The tank was tested with a variety of pressurizations rates of 100 GPa/sec, 10 GPa/sec and 1 GPa/sec. The stress and radial displacement were tracked to determine which pressurization was best for the over-pressurization problem. The desire is a rate that produces minimal material oscillation to eliminate compounding effects for fracture. Of the rates tested, 1 GPa/sec produces the least amount of oscillation and the oscillations it does produce have a low amplitude and long period making them negligible. Thus, the tank is pressurized at a rate of 1 GPa/sec to the point of fracture.

To simulate fracture, the cohesive zone model discussed in Section 3.3.2 is used and the material model is a Johnson-Cook plasticity model. This model has been calibrated to the
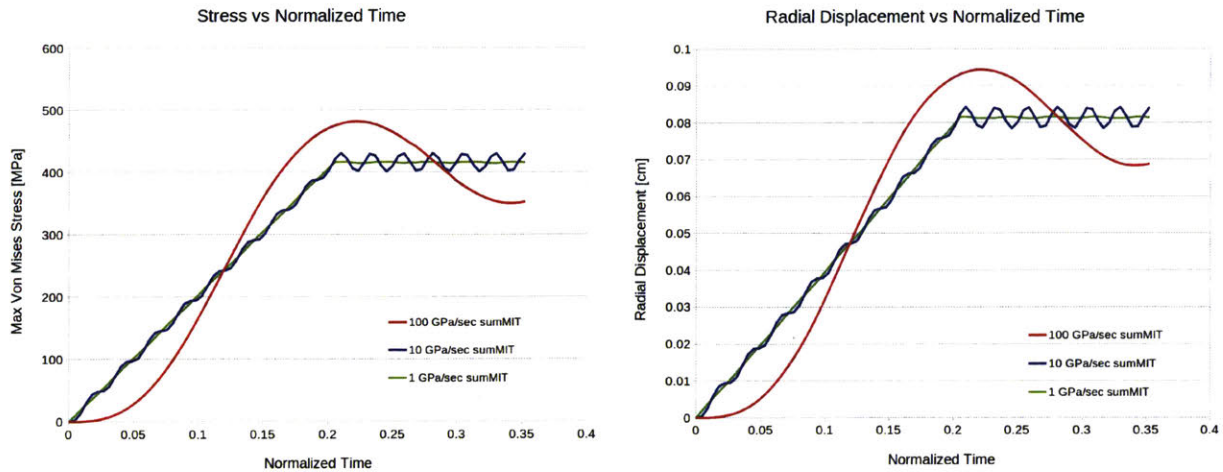
(a) Stress from pressurization

(b) Radial displacement from pressurization

Figure 6-2: Various pressurization rates effect on stress and radial displacement

Parameter	Value
Young's Modulus (GPa)	113.8e9
ν	0.342
A (GPa)	1.09796
B(GPa)	1.09196
$\dot{\varepsilon}_0$	1
C	0.014
n	0.93
m	1.1

Table 6.1: Johnson-Cook parameters for Titanium Ti-6Al-4V

material parameters provided by the Federal Aviation Administration on the material properties of the Johncon-Cook model for Titanium 6Al-4V [32]. Additionally, the basic material properties for Titanium 6Al-4V are obtained from ASM [33]. The material parameters are shown in Table 6.1 and have been converted to SI units.

6.2 Results

As discussed above, the tanks are continuously pressurized past operating levels to a pressure that produces stresses well above the ultimate stress of titanium leading to fracture. Figure 6-3 shows fragmentation of the tank in SUMMIT under these pressurization conditions.

Due to the mesh non-uniformity there are various angles of element interfaces along the hoop of the sphere. Fracture may occur in certain areas of the mesh before other areas because of the angle of element interfaces to the direction of max stress. This can be seen

in Figure 6-3b in the blue zones where fracture has started to occur and stress is being released from the point of the initial crack. Overall, if the mesh interface is perpendicular to the max stress, there is higher likelihood of fracture. This side affect of the mesh creates non-uniform fracture. Additionally, the mass of the overall tank is maintained due to the fracture occurring at the interface, however this leads to single elements or "crumbs" that have broken off of the larger fragments as the pressure continues to rise as shown in Figure 6-3c. The number of crumbs could be reduced by having the pressure reduce or evacuate once fracture initially occurs.

Different meshes and pressurizations create different fracture behavior as can be seen in Figure 6-4. Depending on the meshing, fracture will occur at different locations due to the angle of the elements to the direction of max stress as discussed above.

(a) Prior to fracture
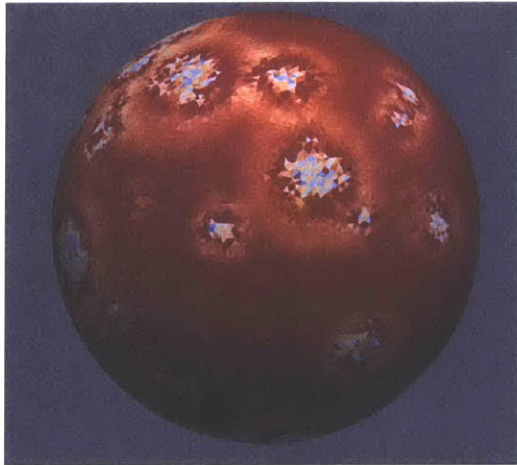
(b) Fracture begins
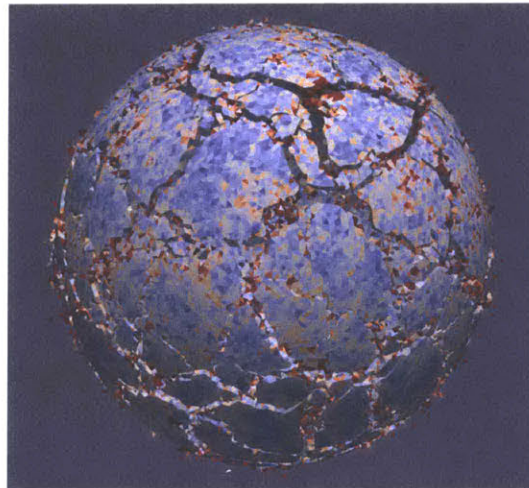
(c) Fracture complete

Figure 6-3: Over-pressurization of 40:1 Titanium tank using Johnson Cook Model with Cohesive Zone Model. In the figures, the von Mises stress is shown with high values in red and low values in blue.

(a) Configuration 2

(b) Configuration 3

(c) Configuration 4

Figure 6-4: Different pressurization and mesh configurations that produce different fracture behavior

Chapter 7

Conclusions

The objective of this research was to develop and calibrate a set of material models that can be used to gain a better understanding of the mechanical response of Roma Plastilina. This task involved simulating three different test configurations and using those configurations to determine a single set of parameters that could be used to classify the Roma Plastilina clay material.
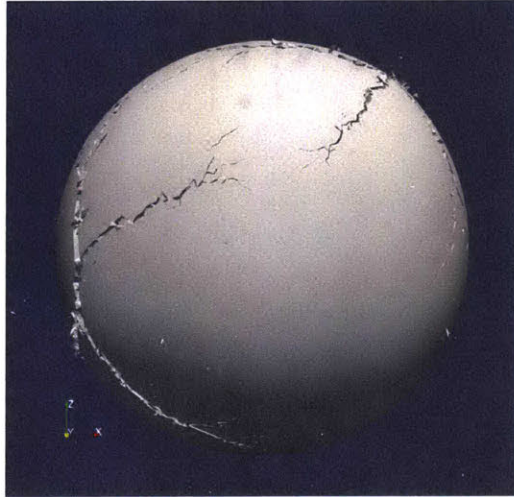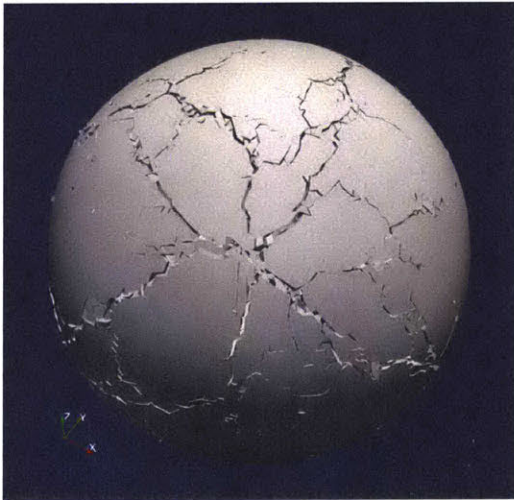
A material model of Cam-clay was used with a rate-dependency modification that aids in the use of one material set for a large range of impact velocities. By replacing the linear rate dependence with a power law rate dependence, the Cam-clay model allows for more flexibility of the rate dependence in the model, thus making the material suitable for any range of strain rates and impact velocities given proper calibration.

Using the power law rate dependence Cam-clay model, as well as the other computational tools, the Cam-clay material model successfully captures the behavior of the drop test and the Threat M. The final depth of the clay is within the range required and the shape of the clay resembles that of the clay as seen in the experiments. The 9mm projectile had a depth that was outside the desired range but still within two standard deviations of the average and therefore is still a reasonable result. The difference in this depth can come from the Dyneema model as the material that is being used does not capture the energy of the impact in the same behavior as in experiments where penetration and then delamination occurs. Although the model of the Dyneema does not capture this behavior, the results of the clay are minimally off demonstrating that these differences are not significant to the Cam-clay

model but rather cause minor changes in the final depth of the clay parameters.

While studying the behavior of the clay and the plate, it was found that the armor separates from the clay early in the impact and thus the clay is behaving based on the energy transfer rather than from the direct contact of the armor. This separation is only noticeable in simulations that are run with discontinuous Galerkin elements with no cohesion between the clay and armor. As discussed in Chapter 4, this idea coincides well with the results seen in the experiments where the final depth of the clay with pads and without are not related by a deformation distance, but rather by an energy absorption level.

Future work on the Roma Plastilina model is related to acquiring more data points of different strain rates or impact velocities that could help to further develop the clay model. More data points would allow for a further calibration of the material. This would help to eliminate gaps within the strain rate range. Additionally, adding these models and parameter sets to the full helmet test protocol would test if the material is properly calibrated.

Applying the cohesive zone model to other problems, the over-pressurization of tanks was also analyzed. For this additional work, the goal was to model fracture of the titanium tank in an over-pressurization case. This case was successfully implemented and tested in which a number of fragments were created and along the crack edges "crumbs" were formed as is expected in fracture of this manner. Although some simulations were successful, there were also cases that had a large amount of ring that occurred when the stress was released which caused oscillation that caused the simulations to crash. Future work on this would need to focus on minimizing the oscillations and providing more stability to the fracture paths. Once the oscillations are minimized, a method for fragment counting and size calculation needs to be implemented in order to start creating a fragment catalog. The pressurized tank work allowed for further application of the cohesive zone model and further work can be done to improve the fracture behavior of metals.

Bibliography

[1] Defense and Veterans Brain Injury Center. Department of Defense Worldwide Numbers of TBI.

[2] C. W. Hoge, D. McGurk, J. L. Thomas, A. L. Cox, C. C. Engel, and C. A. Castro. Mild traumatic brain injury in u.s. soldiers returning from iraq. *New England Journal of Medicine*, 358:453–463, 2008.

[3] Raul Radovitzky. Proposal: Advanced simulation tools to support improvements to helmet testing methodology. Technical report, Massachusetts Institute of Technology, 2017.

[4] Timothy G Zhang, Sikhanda S Satapathy, Lionel R Vargas-Gonzalez, and Shawn M Walsh. Ballistic impact response of Ultra-High-Molecular-Weight Polyethylene (UHMWPE). *Composite Structures*, 133:191–201, 2015. https://doi.org/10.1016/j.compstruct.2015.06.081.

[5] C. Hernandez, M.F. Buchely, and A. Maranon. Dynamic characterization of Roma Plastilina No.1 from Drop Test and inverse analysis. *International Journal of Mechanical Sciences*, 100:158–168, 2015. 10.1016/j.ijmecsci.2015.06.009.

[6] C. Hernandez, A. Maranon, and I. Ashcroft. Inverse methods for the mechanical characterization of materials at high strain rates. *EPJ Web of Conferences – DYMAT 2012 10th International Conference on the Mechanical and Physical Behaviour of Materials under Dynamic Loading*, 26, 2012. 10.1051/epjconf/20122604022.

[7] I. A. Ashcroft C. Hernandez, A. Maranon and J. P. Casas-Rodriguez. Quasi-Static and Dynamic Characterization of Oil-Based Modeling Clay and Numerical Simulation of Drop-Impact Test. In *ASME 2011 International Mechanical Engineering Congress and Exposition Volume 8: Mechanics of Solids, Structures and Fluids; Vibration, Acoustics and Wave Propagation*, pages 147–152. ASME, 2011. 10.1115/IMECE2011-63883.

[8] M.F. Buchely, A. Maranoncor, and V.V. Silberschmidt. Material model for modeling clay at high strain rates. *International Journal of Impact Engineering*, Accepted, 2015. doi:10.1016/j.ijimpeng.2015.11.005.

[9] E. Carton, H. Broos, G. Roebroeks, V. Halls, and J. Zheng. Characterization of dynamic properties of ballistic clay. Technical report, TNO, 2014.

[10] M. Ortiz and A. Pandolfi. A variational Cam-clay theory of plasticity. *Computer Methods in Applied Mechanics and Engineering*, 193:2645–2666, 2004. 10.1016/j.cma.2003.08.008.

[11] Thomas Fronk. Accelerated computational modeling of ballistic helmet test protocols. Master's thesis, Massachusetts Institute of Technology, 2016.

[12] M. Grujicic, G. Arakere, T. He, W. Bell, B. Cheeseman, C. Yen, and B. Scott. A ballistic material model for cross-plied unidirectional ultra-high molecular-weight polyethylene fiber-reinforced armor-grade composites. *Materials Science and Engineering: A*, 498(1):231–241, 2008. https://doi.org/10.1016/j.msea.2008.07.056.

[13] A. Raina and C. Linder. A homogenization approach for nonwoven materials based on fiber undulations and reorientation. *Journal of the Mechanics and Physics of Solids*, 65:12–34, 2014. https://doi.org/10.1016/j.jmps.2013.12.011.

[14] R. Radovitzky and M. Ortiz. Error estimation and adaptive meshing in strongly nonlinear dynamic problems. *Computer Methods in Applied Mechanics and Engineering*, 172(1–4):203–240, 1999. 10.1016/S0045-7825(98)00230-8.

[15] A. Seagraves and R. Radovitzky. *Advances in Cohesive Zone Modeling of Dynamic Fracture*, chapter 12, pages 349–405. Springer, 2009.

[16] O. Ayeni. Test Report for Test Data to Validate Clay Modeling Effort. Technical report, Protective Equipment Test Branch, 2017.

[17] V.P. Kumar and A. Gupta. Analyzing Scalability of Parallel Algorithms and Architectures. *Journal of Parallel and Distributed Computing*, 22(3):379–391, 1994. https://doi.org/10.1006/jpdc.1994.1099.

[18] G. Lyon, R. Kacker, and A. Linz. A scalability test for parallel code. *Software: Practice and Experience*, 25(12):1299–1314, 1995. 10.1002/spe.4380251202.

[19] U.S. Army Research Laboratory DoD Supercomputing Resource Center. Centennial high performance computing system.

[20] A. Schofield and P. Wroth. *Critical State Soil Mechanics*. McGraw-Hill, London, 1968.

[21] M. Ortiz and L. Stainier. The variational formulation of viscoplastic updates. *Computer Methods in Applied Mechanics and Engineering*, 171:419–444, 1999. 10.1016/S0045-7825(98)00219-9.

[22] L. Noels and R. Radovitzky. A general discontinuous Galerkin method for finite hyperelasticity. Formulation and numerical applications. *International Journal for Numerical Methods in Engineering*, 68(1):64–97, 2006. 10.1002/nme.1699.

[23] L. Noels and R. Radovitzky. An explicit discontinuous Galerkin method for nonlinear solid dynamics. Formulation, parallel implementation and scalability properties. *International Journal for Numerical Methods in Engineering*, 74(9):1393–1420, 2007. 10.1002/nme.2213.

[24] R. Radovitzky, A. Seagraves, M. Tupek, and L. Noels. A scalable 3D fracture and fragmentation algorithm based on a hybrid, discontinuous Galerkin, Cohesive Element Method. *Computer Methods in Applied Mechanics and Engineering*, 200:326–344, 2011. 10.1016/j.cma.2010.08.014.

[25] G.T. Camacho and M. Ortiz. Computational modeling of impact damage in brittle materials. *International Journal of Solids and Structures*, 33(20–22):2899–2983, 1996. 10.1016/0020-7683(95)00255-3.

[26] Committee on Review of Test Protocols Used by the DoD to Test Combat Helmets, Board on Army Science and Technology, Division on Engineering and Physical Sciences, and National Research Council. *Review of Department of Defense Test Protocols for Combat Helmets*. National Academies Press, 2014.

[27] Daniel Bürger, Alfredo Rocha de Faria, Sérgio F M de Almeida, Francisco C L de Melo, and Maurício V Donadon. Ballistic impact simulation of an armour-piercing projectile on hybrid ceramic/fiber reinforced composite armours. *International Journal of Impact Engineering*, 43:63–77, 2012. https://doi.org/10.1016/j.ijimpeng.2011.12.001.

[28] S. Min, Y. Chu, and X. Chen. Numerical study on mechanisms of angle-plied panels for ballistic protection. *Materials & Design*, 90:896–905, 2016. https://doi.org/10.1016/j.matdes.2015.11.019.

[29] Yanfei Yang and Xiaogang Chen. Investigation of failure modes and influence on ballistic performance of Ultra-High Molecular Weight Polyethylene (UHMWPE) uni-directional laminate for hybrid design. *Composite Structures*, 174:233–243, 2017. https://doi.org/10.1016/j.compstruct.2017.04.033.

[30] U. Heisserer, H. Van der Werff, and J. Hendrix. Ballistic depth of penetration studies in dyneema® composites. In *Proceedings of the 27th International Symposium on Ballistics April 22-26, Freiburg, Germany*, pages 1936–1943, 2013.

[31] Joseph F. Pittman. Blast and Fragment Hazards from Bursting High Pressure Tanks. Technical Report May, Naval Ordnance Lab White Oak, 1972.

[32] G Kay. Failure Modeling of Titanium 6Al-4V and Aluminum 2024-T3 With the Johnson-Cook Material Model. Technical report, U.S. Department of Transportation - Federal Aviation Adminstation, 2003.

[33] Aerospace Specification Metals, Inc. Titanium ti-6al-4v (grade 5), annealed.

THIS PAGE INTENTIONALLY LEFT BLANK

Appendix A

Constitutive Model of Dyneema

To develop a computational modeling framework for simulating the helmet test protocol, a model of the Dyneema plate response was adopted. The plate tested is made of ultra-high molecular weight polyethylene (UHMWPE) which is built into a composite called Dyneema. This material has been studied at a variety of impact rates and is well characterized within those rates [29, 28]. The Dyneema modeled in this study is a 12" x 12" panel that has 79 plies. To model 79 plies with finite elements, would require a large number of small elements and would not be computationally efficient. For this reason, the Dyneema model of this study has been simplified to aid in the computational time needed to solve the problem. To model the Dyneema, a single ply is used and is modeled using a J_2-flow theory of plasticity with a power-law rate dependence. Although this does not accurately model the penetration of the plate, the back-face shape from the simulations with the computational plate produces results similar to those of the experimental results. In the following sections, the model formulation and the material parameters used for the simulations will be discussed.

A.1   Model Formulation

A.1.1   Governing Equations

Similarly to the Cam-clay governing equations, the deformation gradient is decomposed into an elastic part $\boldsymbol{F}^e$ and a plastic part $\boldsymbol{F}^p$:.

$$\boldsymbol{F} = \boldsymbol{F}^e \boldsymbol{F}^p \tag{A.1}$$

The flow rule is chosen to be a specific form for the J_2-flow theory of plasticity. The flow rule is:

$$\dot{\boldsymbol{F}}^p \boldsymbol{F}^{p-1} = \dot{\varepsilon}^p \boldsymbol{M} \tag{A.2}$$

where $\dot{\varepsilon}^p$ is the effective plastic strain rate. A primary characteristic of the J_2-flow theory of plasticity is that $\boldsymbol{M}$ can be any symmetric tensor that must satisfy the kinematic constraint:

$$\mathrm{tr}(\boldsymbol{M}) = 0 \tag{A.3}$$

$$\frac{2}{3}\boldsymbol{M} \cdot \boldsymbol{M} = 1 \tag{A.4}$$

By restricting attention to isotropic hardening, ε^p is the only internal variable of the material and the free energy becomes:

$$A(\boldsymbol{F}, \boldsymbol{F}^p, T, \varepsilon^p) = W^e(\boldsymbol{C}^e, T) + W^p(T, \varepsilon^p) \tag{A.5}$$

where W^p is the plastic stored energy and W^e is the elastic strain energy density which can be decoupled into the volumetric ,$W^{e,\mathrm{vol}}$, and deviatoric ,$W^{e,\mathrm{dev}}$, elastic responses:

$$W^e(\boldsymbol{C}^e, T) = W^{e,\mathrm{vol}}(\det(\boldsymbol{F}^e), T) + W^{e,\mathrm{dev}}(J^{e-2/3}\boldsymbol{C}^e, T) \tag{A.6}$$

where $\det(\boldsymbol{F}^e)$ is the Jacobian of the elastic deformation and $J^{e-2/3}\boldsymbol{C}^e$ is the deviatoric elastic right Cauchy-Green deformation tensor.

The equation of state for the J_2-flow theory of plasticity can be given by Equation (A.7)

with the assumption that the isothermal bulk modulus and specific heat at constant volume are constant.

$$W^{e,\mathrm{vol}}(J^e, T) = \frac{K}{2}[\theta^e - 3\alpha_T(T - T_0)]^2 + \rho_0 C_v T\left(1 - \log\frac{T}{T_0}\right) \tag{A.7}$$

where K is the isothermal bulk modulus, α_T is the thermal expansion coefficient, T_0 is a reference absolute temperature, ρ_0 is the mass density per unit undeformed volume, and C_v is the specific heat per unit mass at constant volume. And the deviatoric elastic strain-energy is given by Equation (A.8) with μ being the shear modulus and e^e is the deviatoric logarithmic elastic strain.

$$W^{e,\mathrm{dev}} = \mu|e^e|^2 \tag{A.8}$$

By discretizing the system, incremental deformations can be solved for in $\triangle t$ time steps. An incremental energy function using logarithmic elastic strains is defined [21, 14]:

$$f_n(\boldsymbol{F}_{n+1}, T_{n+1}; \varepsilon_{n+1}^p, \boldsymbol{M}) =$$

$$W^e(\boldsymbol{F}_{n+1}^e, T_{n+1}) + W^p(T_{n+1}, \varepsilon_{n+1}^p) + \triangle t\,\psi^*(\triangle\varepsilon^p/\triangle t) \tag{A.9}$$

where ψ^* is the dual kinetic potential that will later be given and is used to determine the rate-sensitivity of the material. The effective work-of-deformation density can be defined by minimizing f_n with respect to the effective plastic strain, ε_{n+1}^p, and direction of plastic flow, $\boldsymbol{M}$:

$$W_n(\boldsymbol{F}_{n+1}, T_{n+1}) = \min_{\varepsilon_{n+1}^p, \boldsymbol{M}} f_n(\boldsymbol{F}_{n+1}, T_{n+1}; \varepsilon_{n+1}^p, \boldsymbol{M}) \tag{A.10}$$

and is subject to a plastic irreversibility constraint:

$$\triangle\varepsilon^p = \varepsilon_{n+1}^p - \varepsilon_n^p \geq 0 \tag{A.11}$$

According to [21, 14], the effective work-of-deformation acts as a potential for the first Piola-Kirchhoff stress tensor in the form:

$$\boldsymbol{P}_{n+1} = \frac{\partial W_n}{\partial \boldsymbol{F}_{n+1}}(\boldsymbol{F}_{n+1}, T_{n+1}) \tag{A.12}$$

And the tangent moduli from the linearization of Equation (A.12) results in the symmetric tensor,

$$DP_{n+1} = \frac{\partial^2 W_n}{\partial F_{n+1} \partial F_{n+1}}(F_{n+1}, T_{n+1}) \tag{A.13}$$

After expressing the elastic strain energy in terms of logarithmic elastic strains and following similar steps as above, the following stress equation is defined:

$$\sigma(\varepsilon_{n+1}^{pre}) = \sigma_c(\varepsilon_{n+1}^p) + \frac{9}{2}\mu \triangle \varepsilon^p + \psi^{*\prime}(\triangle \varepsilon^p / \triangle t) \tag{A.14}$$

which can be solved for the unknown ε_{n+1}^p using a Newton-Raphson iteration under the irreversibility constrain (A.11). Using the calculated value, the stresses can be updated.

A.1.2 Power Law assumptions

For the material to be considered a J_2-flow theory of plasticity with power-law, a power-law form needs to be assumed for both hardening and rate-sensitivity. The stored energy function for the power-law is:

$$W^p = \frac{n\sigma_0(T)\varepsilon_0^p}{n+1}\Big[1 + \Big(\frac{\varepsilon^p}{\varepsilon_0^p}\Big)\Big]^{(n+1)/n} \tag{A.15}$$

where n is the hardening exponent, ε_0^p is a reference plastic strain, and $\sigma_0(T)$ is the flow stress with an assumed thermal-softening law:

$$\sigma_0(T) = \sigma_y\Big(1 - \frac{T}{T_m}\Big)^l \tag{A.16}$$

where σ_y is the yield stress, T_m is the melting temperature, and l is the thermal softening exponent. The dual kinetic potential used to determine the rate -sensitivity of the material is defined by:

$$\psi^* = \frac{m\sigma_y\dot{\varepsilon}_0^p}{m+1}\Big[1 + \Big(\frac{\dot{\varepsilon}^p}{\dot{\varepsilon}_0^p}\Big)\Big]^{(m+1)/m} \tag{A.17}$$

where m is the rate-sensitivity exponent, $\dot{\varepsilon}_0^p$ is the reference plastic strain and σ_y is the yield stress.

Appendix B

Summary of Contact Algorithm

Figure B-1 depicts the various elements needed for the contact algorithm. The contact algorithm uses the mesh object and the impactor and produces an interpenetration zone by giving a radius, r, away from the impact node. At each time step, the contact algorithm checks every quadrature point on the surface and determines if the impactor is in contact with the quadrature point. A quadrature point is in contact if the distance, d, between the quadrature point and the contact node is less than the radius. If the distance is less than the radius then the quadrature point is in contact and a residual contact force is determined. The contact force is determined using Equation (B.1) in which δ is the difference between the radius and the distance between the two points. This penalty contact force is applied to the quadrature point. Then this process is repeated for every quadrature point along the surface and then the resulting contact forces are assembled into one global force vector and that global force vector is applied to the contact node. This step by step process is shown in Figure B-2 as it occurs at each time step.

$$F_{penalty} = \delta * p \tag{B.1}$$

The penalty parameter, p, determined the resulting initial magnitude of the contact force and is calibrated for a given problem. The penalty parameter determines the amount of contact force that is generated by the contact of two objects. If the penalty parameter is too low, the impactor will not have a high enough stopping force causing interpenetration
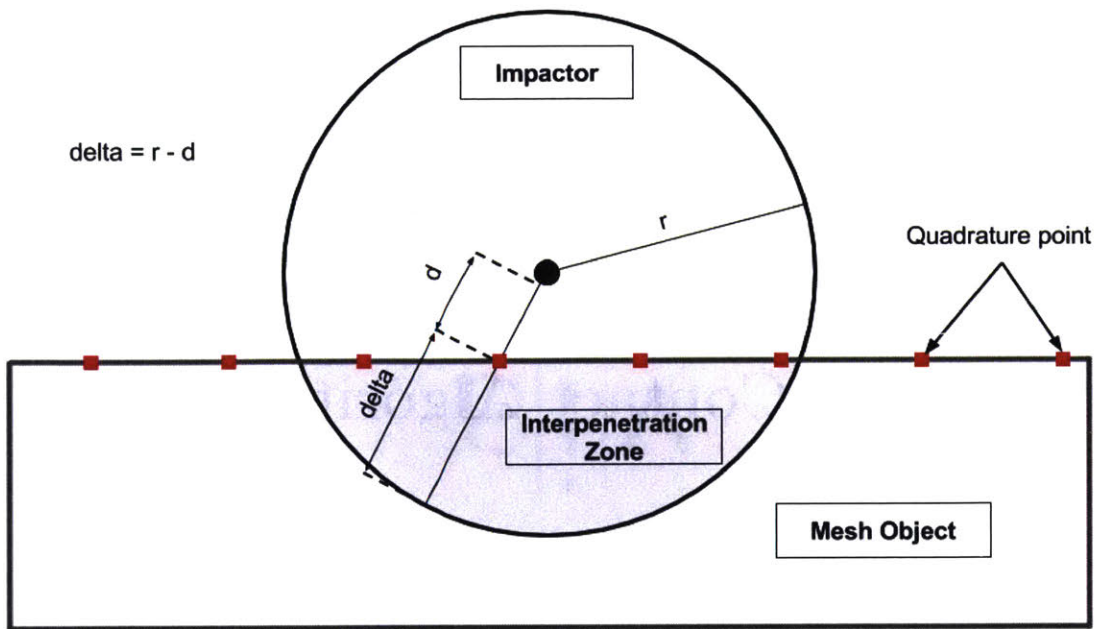
Figure B-1: Illustration of the penalty contact algorithm objects and variables [11]

of material and a penalty parameter that is too high will create too large of a force leading to inaccurate results.
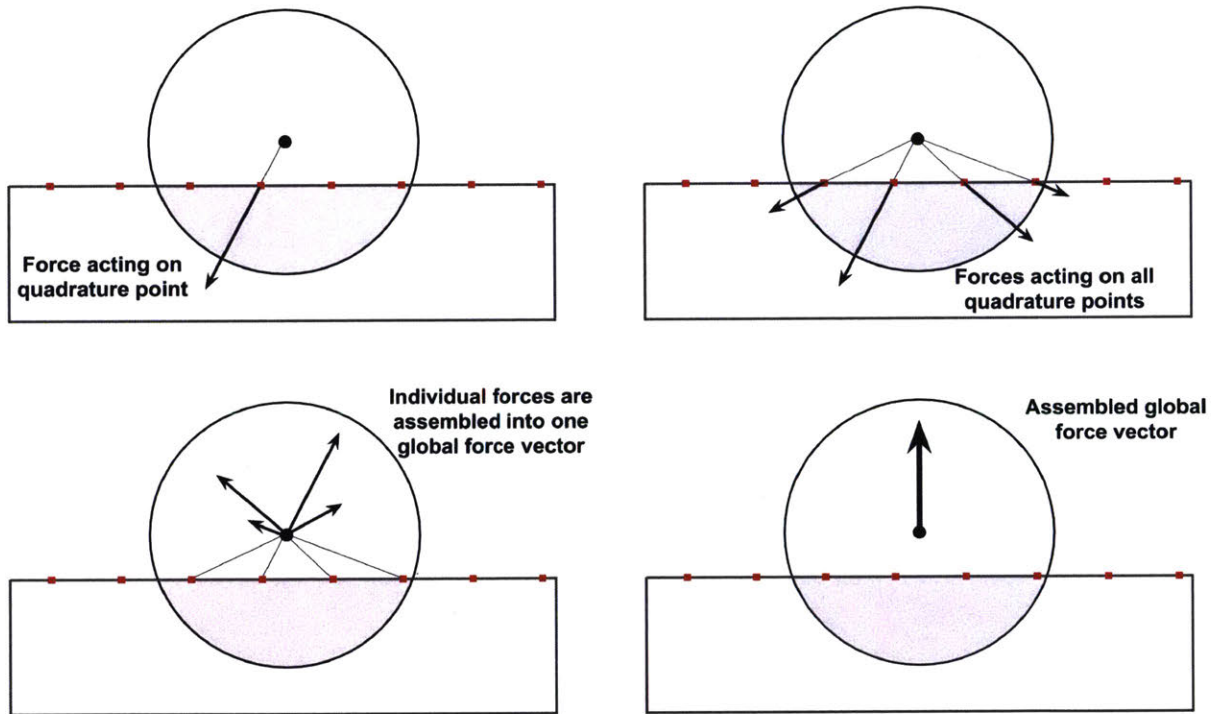
Figure B-2: Process of the penalty algorithm for contact of the impactor and the mesh surface [11]